Fracture Mechanics Approach to Splitting in Low Spring Index Cold Coiling Process

Y. Prawoto[a)], S. Manville [a)], S. Tadashi [a)] L. Lee [a)], M. Tanaka [b)] and T. Gnauple-Herold [c)]

[a)]*NHK International Co. 46855 Magellan Dr. Novi MI 48377*

[b)]*NASCO Spring USA, 3251 Nashville Road, Bowling Green, KY 42101*

[c)]*NIST Center For Neutron Research, 100 Bureau Dr. Gaithersburg, MD 20899*

Abstract

This paper is an attempt to understand the coil splitting phenomena by means of fracture mechanics. The methods used combines the residual stress measurement with neutron and finite element analysis. The support of the metallurgical evaluation is used as an evidence to justify the use of fracture mechanics concept. Comparing coil springs manufactured at two different manufacturing lines, namely N1 and N6, residual stress distributions in three main directions were measured using neutron diffraction. The results of the residual stress measurement were then converted to the stress intensity factor to enable the analysis in fracture mechanics. The mixed mode analysis of opening, Mode I, and in-plane shearing, Mode II, is used to solve the splitting problem.

The discrepancy between the coil made at N1 and N6 was identified and taken into account in terms of the profile difference. Based on this difference, an FEA simulation was conducted. The results support the experimental finding, which is that the shape of the coil manufactured influences the pattern of the residual stress, which leads to different splitting behavior. This simple analysis helps practitioners understand why, and how, some cold coiled products split after manufacturing. It is concluded that this very basic concept of fracture mechanics can be used to establish the limit of the cold coiling process by evaluation of the mixed mode stress intensity factor to the fracture toughness of the material.

Keywords: Residual stress, Neutron Diffraction, Cold forming, Stress Intensity Factor, *J*-Integral

1. Introduction

Spring index is the ratio between the mean diameter of a spring and the wire diameter of a spring. It has been known that this proportion determines the strength of the spring, the stress induced on the spring, and the manufacturability of the spring.

By conventional manufacturing methods, typically a spring index up to 3.9 cannot be manufactured, while a spring index between 4 to 5 falls in the difficult to manufacture category due to too much stress on the tooling and higher possibility in cracking during the manufacturing process, resulting in higher cost to manufacture. A spring index in the range of 6 to 12 is the preferred choice for coil manufacturers. Above 12, tolerance becomes an issue and coil manufacturers typically cannot meet the drawing provided by the design engineers[1].

Meanwhile, the demand of weight reduction in the automotive industry forces suspension spring manufacturers to use higher strength steel. The traditional approach in forming such materials is based on hot coiling of the wire at temperature higher than the AC_3 line to increase material formability while the material is still in austenite form. This method has been used for decades and has been proven to minimizing required forming forces. Recent development however, is to manufacture the coil spring by cold forming. In the cold forming process, advantages include improved shape because heat treatments can be performed elsewhere prior to the spring being formed. In cold coiling, material is formed directly in its final condition, typically tempered martensite. Consequently, the coiling process becomes more critical because the formability of these high-strength martensitic steel is usually low compared to austenite in the case of hot coiling.

Nowadays, the high strength steel used for suspension coil spring material is even moving further in the direction of much more high strength up to 2100MPa, although in the market usually 1800MPa is about the limit. Even at this level, the cold forming of the wire can be extremely difficult, triggering manufacturing failure caused by the breakage of the spring and splitting. These types of problems for some manufacturers that use hot coiling could be troublesome. Similar problems in cold coiling are also reported in several other publications[2,3]. In their paper, Matejicek *et.al*[3] used neutron diffraction and found that the residual stress is mainly responsible for splitting.

This paper discusses a particular problem in the cold coiling process where the coil splits along the wire either soon after coiling or sometime in between the coiling process and the end of the stress relief annealing process. The approach used here concentrates on the effect of residual stress since cracking takes place after the coiling process is complete, similar to that of Matejicek's *et.al*[3]. To do this, we mimic his approach combined with finite element method, metallurgy, and fracture mechanics. The approach of quantitative analysis is preferred here with the hope that this would initiate better research in understanding the phenomena.

2. Theory

To approach the problem, basic knowledge of fracture mechanics is used. The residual stress is converted to a stress intensity factor and subsequently used to analyze the splitting. In this case, Mode I and Mode II are used in the analysis simultaneously, instead of the *J*-Integral concept that is more suitable for softer materials[4]. Since the material is very hard and brittle, as it is discussed in the metallography section, the approach to use the stress intensity factor is fully justified. Recall that the stress intensity factor, *K*, is used in fracture mechanics to predict the stress state near the tip of a crack caused by a remote load or residual stresses. It is a theoretical idea applied to a homogeneous, linear elastic material and is useful for providing a failure criterion for brittle materials; it is a favorite technique in the discipline of damage tolerance. The value depends on sample geometry, the size and location of the crack, and the magnitude and modal distribution of loads on the material. The stress state near the crack

$$\sigma_{ij}(r,\theta) = \frac{K}{\sqrt{2\pi r}} f_{ij}(\theta) \tag{1}$$

where

K is the stress intensity factor

f_{ij} is a dimensionless quantity that varies with load and geometry

In our case, the Mode I and Mode II respectively is

$$K_I = \lim_{r\to 0} \sqrt{2\pi r}\, \sigma_{yy}(r,0) \tag{2a}$$

$$K_{II} = \lim_{r\to 0} \sqrt{2\pi r}\, \tau_{xy}(r,0) \tag{2a}$$

The failure criterion in this case, is taken as

$$K_c \leq \sqrt{K_I^2 + K_{II}^2} \tag{3}$$

where K_c is the material fracture toughness. This approach is believed to be much better and more suitable than the conventional failure criteria, such as Tresca or Von Mises failures[5,6].

3. Experiment

Material selected was SAE 9254, due to its popularity both in cold coiling and hot coiling processes[7]. Two different coil springs, manufactured at two different coil machines, are used for study. Figure 1 shows a typical coil machine for cold coiling process. The forming cycle varies from 6s-10s and the formed spring requires a simple setting stage without further heat treatments, except a stress relief annealing. The machine is a numerical programmable system, consisting of wire feeder roll where the wire is straightened and fed from the bundle to the wire guide. The wire guide passes the wire to the first forming roll where the first coiling process takes place. The second forming roll and the pitch bar work synergistically to form the coil into desired shape. Both the pitch bar and the roll are controlled by programs and servo systems. Here the coil pitch and the diameter is shaped to the desired dimension. Once the coil forming is finished,

the upper shear will move down to cut the wire. It is worth noting that shearing also introduces energy to the system that indirectly contributes to the initiation of the splitting.

The usage of two forming rolls allows reduction in the friction between the wire and the forming tools and therefore the required forming force is also reduced. After this, the coil is sent to the next process, which is stress relief anneal. Residual stress remaining during coiling is mostly eliminated during this process. Occasionally, the coil splits after the coiling process. Figure 2 shows the representative appearance of such phenomena. It is the suspicion that this is due to excessive residual stress created during coiling. The evaluation items are limited to FEA simulations, neutron diffraction and X-ray residual stress measurement, and metallurgical evaluation.

FEA Simulations

Figure 3 shows the initial set up of the model. The model mimics the real experiment, where the wire with ta diameter of 14.9mm is fed into the wire-feeder and eventually shaped into a coil using Roller 1 and Roller 2. Both rollers are constrained as rigid bodies having a 0.1 friction coefficient relative to the wire. The rollers can spin with respect to its center axles with a friction coefficient of 0.3 relative to the axles. The friction coefficient between the wire and the wire-guide is also 0.3. This variation of the friction coefficient is able to produce a similar situation with the experiment where the angular displacement at the surface of the roller is slower than wire displacement due to the wire being pushed.

In the initial set up, the tip of the wire is already coiled 135^{o}. The simulation is started with pushing the tip of the opposite end so that plastic deformation takes place on the originally straight wire to form coil. For this particular analysis, a convergence test was performed and a mesh size of 1.5mm at the straight part and 2mm at the curved part were concluded to have converged results. The analysis used *Abaqus*^{TM} with a meshing type of C3D20 Quadratic brick with reduced integration. The material constants used were to follow those of SAE9254 at 23^{o}C with the strain rate of 0.0 and 0.278. The information from the drawing was used. Profiling the actual coil shapes obtained in experiment made it possible to differentiate the simulation of N1 and N6 coils. In this section, the only difference between N1 and N6 is the coil profiles. The coil profiles were measured experimentally.

In general, the procedure consists of two steps. The first step is to feed the wire until an addition of more than 180^{o} of new coil is formed. In this step, it simulates coil manufacturing where energy supplied to the system is used to plastically bend the wire, slip the wire to the roller and to rotate the rollers. The first step is ended by stopping the displacement of the left end of the wire. This first step left the system in an elastic equilibrium of the wire giving compression to the roller. The second step is to move the rollers away from the wire leaving the wire in the coil shape. At this step, the spring-back of the coil due to the removal of elastic compression experienced by the wire to the rollers takes place. Consequently, the coil shape is changed from the original shape obtained in step 1. The simulation is completed after the second step.

The change from the straight wire to coil basically takes place in a mixture of compression and tension inside the system. Furthermore, the degree of the plastic deformation also varies significantly. As a result, the system consists a variation of residual stress due to new equilibrium of the wire being in the shape of a coil. The analysis result is extracted as remaining stress in all elements. With some coordinate

manipulations, the results are presented here. Figure 4 shows the result of the tangential residual stress, which is the residual stress in the wire direction. It is like what we expect the longitudinal stress distribution to be, as the stress in this direction is the remaining stress of the applied bending moment in classical mechanics:

$$\sigma_T = \frac{My}{I} \tag{4}$$

where σ_T is the tangential/hoop stress, M is the applied moment, y is the distance from the neutral axis and I is the moment of inertia of circular cross section, $\pi r^4/4$. According to Equation (4), the applied stress due to the moment given during coiling would become tension at the outer diameter of the bending and compression at the inner. Figure 5 illustrates the estimate of tangential residual stress. In order to make the system in both force and moment balance, an imaginary negative moment is introduced. A similar concept can be used to comprehend the radial direction of stress, shown in Figure 6. In the case of stress in the radial direction, the problem becomes similar to that of a thick walled cylinder problem where stress in the radial direction is formulated by:

$$\sigma_r = \frac{E}{1-\nu^2}\left(\frac{du}{dr} + \nu\frac{u}{r}\right) \tag{5}$$

where σ_r is the radial stress. The term $\left(\frac{du}{dr}\right)$ is actually the radial strain, ε_r. Equation (5) for our system cannot be solved easily since they form partial differential equations that involves two constants that require two boundary conditions with a difference is too small to be even considered. This direction of stress is usually neglected. However for this particular investigation, this stress is not neglected despite its small amount, a maximum about 50 MPa. This is far from the tangential stress value, which is above 1000MPa. The radial direction of residual stress here is computed because it relates directly to Mode I failure discussed in Equation (2a) and eventually in Equation (3).

More significantly is the shear stress at the same location. The shear stress is related directly to Equation (2b), which is Mode II in fracture mechanics and eventually to Equation (3). Figure 7 shows the distribution of the residual shear stress. This is the most important aspect in this research since Mode II is also the factor that contributes to the splitting along, with Mode I as it is shown in Equation (3). Figure 8 can be understood by the concept of shear stress in beam classical mechanics:

$$\tau_T = \frac{V}{I\,b}\int_{y0}^{c} y\,da \tag{6}$$

where τ_T is the shear stress, V is the applied shear load which in our case is $V = \frac{dM}{dx}$. Recall that M is the applied moment used in Equation (4), y is the distance from the neutral axis, and I is the moment of inertia of circular cross section, $\pi r^4/4$, while b is the width. The integral part would be in the form of first moment, which is the area of wire cross-section. Similar with how Figure 6 was established, one can establish illustration to estimate the distribution of the residual shear stress. While all figures from Figure 3 until Figure 7 describe the general analysis results, the discrepancy between N1 and N6 is shown in Figure 8. In Figure 8, the tangential/hoop residual stress of N1 is shown to be slightly larger than that of N6. Similar trends are also found on the radial direction and the shear stress. It is worth noting here that some of the results are not accurate since in principle the following concepts remain true:

$$\sum F = 0 \qquad \text{and} \qquad \sum M = 0 \tag{7}$$

Therefore, when using the results described in Figure 8, one needs to be careful as they may not be accurate quantitatively in their numerical values, but rather should be taken qualitatively. In this research, the values of the residual stresses are converted into residual stress intensity factors, which enables us to make better explanation as to why the splitting happens and further as to why the N1 coil has higher a probability to split than the N6 coil.

Neutron and X-ray Diffraction Analyses

The measurement of residual stress with neutron diffraction is based on measurements of changes in crystal lattice spacing, which manifests themselves as shifts in angular position of respective diffraction peaks, according to Bragg's law:

$$n \cdot \lambda = 2d \sin\theta \tag{8}$$

where

n is the reflection order

λ the radiation wavelength

d the plane spacing, and

θ is the diffraction angle.

The strain can then be computed by:

$$\varepsilon = \left(\frac{d-d_0}{d_0}\right) \tag{9}$$

where

ε is the strain in a particular direction

d the stressed, and d_0 the unstressed interplanar spacing

The stress components can be calculated as:

$$\sigma_{11} = \frac{E}{(1+v)(1-2v)}[(1-v)\varepsilon_{11} + v(\varepsilon_{22} + \varepsilon_{33})] \tag{10a}$$

$$\sigma_{22} = \frac{E}{(1+v)(1-2v)}[(1-v)\varepsilon_{22} + v(\varepsilon_{11} + \varepsilon_{33})] \tag{10b}$$

$$\sigma_{33} = \frac{E}{(1+v)(1-2v)}[(1-v)\varepsilon_{33} + v(\varepsilon_{11} + \varepsilon_{22})] \tag{10c}$$

In our case, σ_{11} is the stress in tangential direction, while the σ_{22} is the stress in the radial direction, see Figure 9. The gage volume for this measurement was 1.5mm x 1.5mm x 1.5mm. Figure 10a and Figure 10b show the measurement results. The tendency of the residual stress measured by neutron diffraction is similar to that of the FEA computational results. However, the residual shear stress can only be calculated and not measured by neutron diffraction.

To compare the measurement results with the FEA results, one can pick the most obvious measurement results, which are tangential residual stress. In Figure 8, the peak of the residual stress is about 1000-1100MPa, while in Figures 10a and 10b they are about 800-900MPa. Recall that our gage volume for measurement was 1.5^3 [mm^3], or 3.375 mm^3. In this volume of the gage, using our material that has grain size of 10, we average approximately 4.85 million prior austenite grains. Therefore, in this case, residual stress value is always an underestimation, because the gage size is much larger than the size of the peak.

Metallurgical Evaluation

Metallurgical evaluation is focused on the tip of the cracks. On the samples manufactured at N1 and N6, approximately 200mm length of coils were sectioned and mounted carefully into transparent lucite. The samples were subsequently ground and polished. During polishing, both samples split at a location almost identical with what happened to other coils that split after cold coiling. Figure 11 shows the appearance. The same figure also shows the mapping of micro hardness. No significant difference between the two coils were found from this evaluation. The spectrum of the hardness of the N6 sample seems broader than that of N1 sample. However, this is very common discrepancy since the samples are not annealed.

With this, Figure 11 shows the condition at the crack tips for both the N1 and N6 samples. The figure shows that the N1 sample has straighter crack compared with the N6 sample. The N6 sample has many more crack branches than the N1 sample. This implies that the stress of N1 is higher than the stress in N6. Figure 12 shows the enlargement of the crack path at a selected location. This figure is used as a tool to determine which modes were involved in the cracking. One can see the tendency of the cracking mode to be mixed between Mode I and Mode II, as they are indicated by red arrows. In the figure, the red arrows show the vectors of translation from points that were originally adjacent. This proves that the cracking was indeed the combination of Mode I and Mode II. Regular proof of grain elongation could not be observed due to the sample being hardened. This fact justifies the use of the stress intensity factor concept rather than *J*-Integral concept.

4. Discussion

In this research, qualitatively one can get the idea that excessive residual stress caused the splitting to take place after the cold coiling process. However, to what extent the residual stress caused the splitting remains unexplainable, since classical mechanics only states that if the Von Mises stress is lower than the UTS, no splitting can ever take place. If the generalized concept is used, the maximum average stress would never crack the sample, given the fact that the residual stress value is not even 80% of the material's ultimate tensile strength.

In this research, the idea is to get an explanation of why the splitting takes place only with residual stress. To do that, the stress intensity factor is brought in. Furthermore, the concept of weight function is also adopted in converting the residual stress to residual stress intensity factor.

$$K_I = \int_0^a \sigma^R(x) h_I(x,a) dx \qquad (11a)$$

and

$$K_{II} = \int_0^a \tau^R(x) h_{II}(x,a) dx \quad (11b)$$

where $\sigma^R(x)$ and $\tau^R(x)$ are the normal residual stress and the shear residual stress along the crack prospective line, respectively. K_I and K_{II} are Mode I and Mode II stress intensity factors and $h_I(x,a)$ and $h_{II}(x,a)$ are the weight functions that depend solely on the geometry[8–10]. Generally the value of the weight function is computable through:

$$h(x,a) = \frac{H}{K(a)^{(1)}} \frac{\partial u^{(1)}(x,a)}{\partial a} \quad (12)$$

H is E for plane stress condition and $\frac{E}{1-v^2}$ for plane strain condition. $K(a)^{(1)}$ and $u^{(1)}(x,a)$ are respectively the known stress intensity factor and the crack face displacement. To find those, the help of FEA was utilized. A model to mimic this was created, subsequently the stress intensity factor, $K^{(1)}$ is calculated and the displacement function $u^{(1)}$ was also obtained. For this purpose, the computation was via J-Integral and the following relation is used.

$$J = K^2 \frac{(1-v^2)}{E} \quad (13)$$

To obtain the value of the parameters needed, analysis shown in Figure 13 was performed. From this analysis, the correlation of the displacement behind the crack, the crack face displacement, $u^{(1)}(x,a)$ was obtained. At the same time, the corresponding $K(a)^{(1)}$ was also obtained. The analysis to simulate both Modes I and II were performed by giving dummy displacements of unity. Subsequently, the relation of the displacement vs. stress intensity factor can be obtained in the four degree polynomial for Mode I as:

$$h_I(x,a) = \frac{H}{K(a)^{(1)}} 0.048 + 0.0008a - 0.0012a^2 - 0.0846x + 0.08ax \quad (14a)$$

While for Mode II is:

$$h_{II}(x,a) = \frac{H}{K(a)^{(1)}} 0.0828 - 0.0188a + 0.0021a^2 - 0.007x + 0.0066ax \quad (14b)$$

The above empirical equations were obtained by analytical program, Mathematica™ -- three dimensional curve fitting into three degree polynomial followed by partial differential with respect to $h_I(x,a)$. Recall that the above equations are related directly to Equations (11a and 11b).

The idea of bringing the metallurgical concept into the solid mechanics world is always fascinating. In this research, one can see that both Mode I and Mode II contributed to the splitting, as it is seen in Figure 13. Furthermore, if the red arrow in the corresponding figure can be used as a vector for the fracture surface creation and separation, vector algebraic addition law should be applicable. Therefore, at the crack length of 8cm our combined stress intensity factor becomes:

$$K = \sqrt{K_I^2 + K_{II}^2} \quad (15)$$

where $K_I$and K_{II} respectively can be calculated using the weight functions and FEA analysis of $K(8)_I^{(1)} = 22{,}918$ and $K(8)_{II}^{(1)} = 3103$,

$$K_I = \int_0^8 \frac{E}{(1-\nu^2)22{,}918}(-0.02 + 0.556\,x)\sigma^R(x)dx \quad (16a)$$

and

$$K_{II} = \int_0^8 \frac{E}{(1-\nu^2)3{,}103}(0.198 + 0.043\,x)\tau^R(x)dx \quad (16b)$$

Knowing the material's Young modulus and Poisson's ratio, combined with $\sigma^R(x)$ and $\tau^R(x)$ from the neutron diffraction measurement and FEA modeling, Equations (16a) and (16b) can be calculated to become:

$$K_I = \frac{202{,}815}{20{,}855}(-0.6x + 8.34\,x^2)\Big|_0^8 = 5144 \quad (17a)$$

$$K_{II} = \frac{202{,}815}{2{,}823}(79.2\,x + 8.60\,x^2)\Big|_0^8 = 85{,}063 \quad (17a)$$

$$K = 85{,}218 \quad (18)$$

Note that the above equations were calculated by considering the results that at the crack prospective line, the value of $\sigma^R(x)$ is 30 MPa and $\tau^R(x)$ is 400 MPa constant, while the Young's modulus E is 202.815GPa and Poisson's ratio of 0.3. Equations (17a) and (17b) clearly shows that the influence of the shearing is indeed much larger than that of normal stress. It is worth noting that the shear stress value can also be obtained by derivation of normal stress in the longitudinal direction. In doing the calculation, the help of Abaqus was also utilized here.

After the unit conversion, Equation (18) can be directly compared with experimental fracture toughness. Here, the value of in SI unit $K = 85.2\ MPa\sqrt{m}$. This can be considered as a critical value because if the material used has a fracture toughness lower than this value, e.g., high hardness, the material would be more prone to the splitting. The same material that has higher toughness, e.g., low hardness, would therefore be less prone to the splitting.

5. Conclusion

Springs manufactured at two different coil machines were selected for study. Fracture mechanics theory was used to understand the phenomena. The splitting in this case took place in the lab several days after manufacturing. Based on the crack tip evaluation, it was concluded that the cause for the splitting was due to normal stress acting to separate fracture surface and in-plane shear stresses acting synergistically. Here, metallurgy was used as a quantitative method to justify the introduction of mixed mode fracture mechanics. The fracture mechanics concept was subsequently used to establish a critical-boundary value between non-propagating or propagating cracks. It was shown that this boundary corresponds to fracture toughness value.

Reference:

1. Childs, P. R. N. *Springs*. *Mechanical Design Engineering Handbook* (2014). doi:10.1016/B978-0-08-097759-1.00015-0

2. Guido, B. & Manuel, M. Experimental and numerical analysis of the cold forming process of automotive suspension springs. 1–18 (2011).

3. Matejicek, J., Brand, P. C., Drews, A. R., Krause, A. & Lowe-Ma, C. Residual stresses in cold-coiled helical compression springs for automotive suspensions measured by neutron diffraction. *Mater. Sci. Eng. A* **367,** 306–311 (2004).

4. Prawoto, Y. & Onn, I. H. Application of J-integral concept on blister coating problem. *Eng. Fract. Mech.* **92,** 114–125 (2012).

5. Chao, Y. J. Ultimate Strength and Failure Mechanism of Resistance Spot Weld Subjected to Tensile, Shear, or Combined Tensile/Shear Loads. *J. Eng. Mater. Technol.* **125,** 125 (2003).

6. Qu, R. T., Zhang, Z. J., Zhang, P., Liu, Z. Q. & Zhang, Z. F. Generalized energy failure criterion. *Sci. Rep.* **6,** 1–8 (2016).

7. Vilela Costa, L., Gonçalves Carneiro, J. R., Pinto Coelho Catalão, R., Ribas, O. K. & Brito, P. Residual Stress Gradients in AISI 9254 Steel Springs Submitted to Shot Peening and Heat Treatment for Increased Fatigue Resistance. *Adv. Mater. Res.* **996,** 749–754 (2014).

8. Fett, T., Tilscher, M. & Munz, D. Weight functions for cracks near the interface of a bimaterial joint and application to thermal stresses. *Eng. Fract. Mech.* **56,** 87–100 (1997).

9. Fett, T. Stress intensity factors and weight function for a void with an annular crack. *Int. J. Fract.* **67,** (1994).

10. Coules, H. E., Horne, G. C. M., Abburi Venkata, K. & Pirling, T. The effects of residual stress on elastic-plastic fracture propagation and stability. *Mater. Des.* **143,** 131–140 (2018).

Figures:

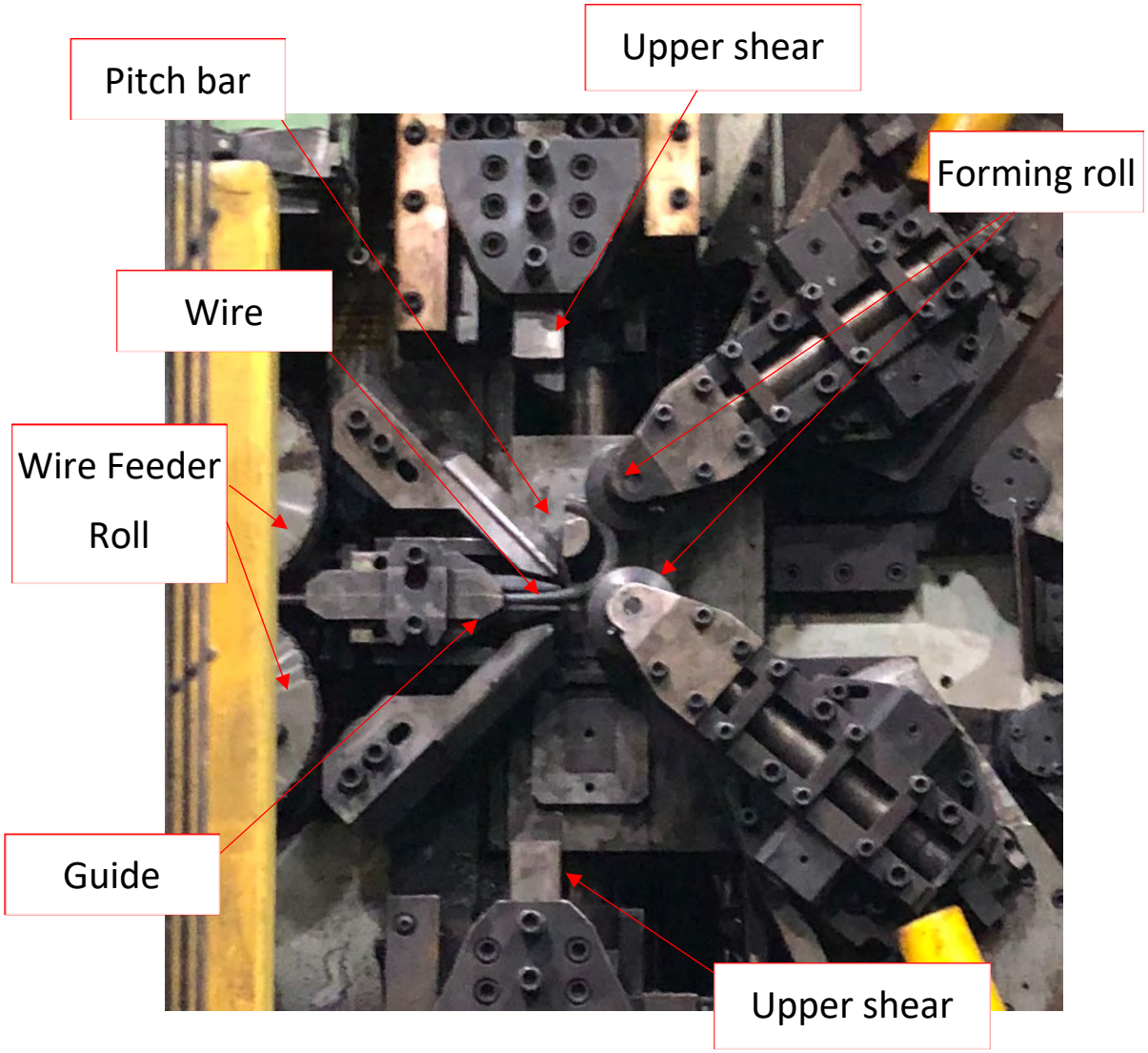


Figure 1. Cold Coiling Machine

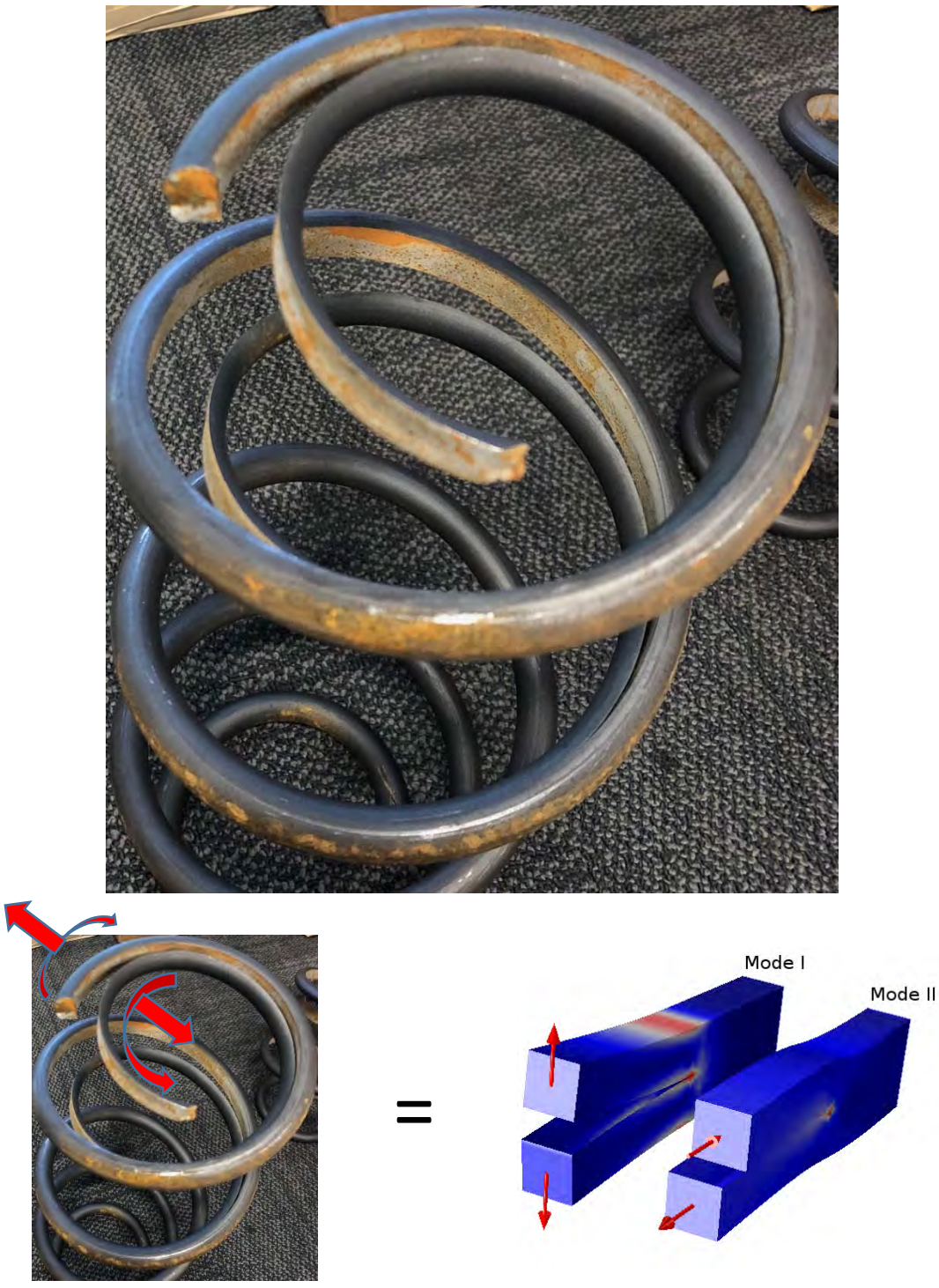


Figure 2. Appearance of the splitting that takes place after coiling before stress relief annealing. The figure also shows the concept for the usage of mixed mode.

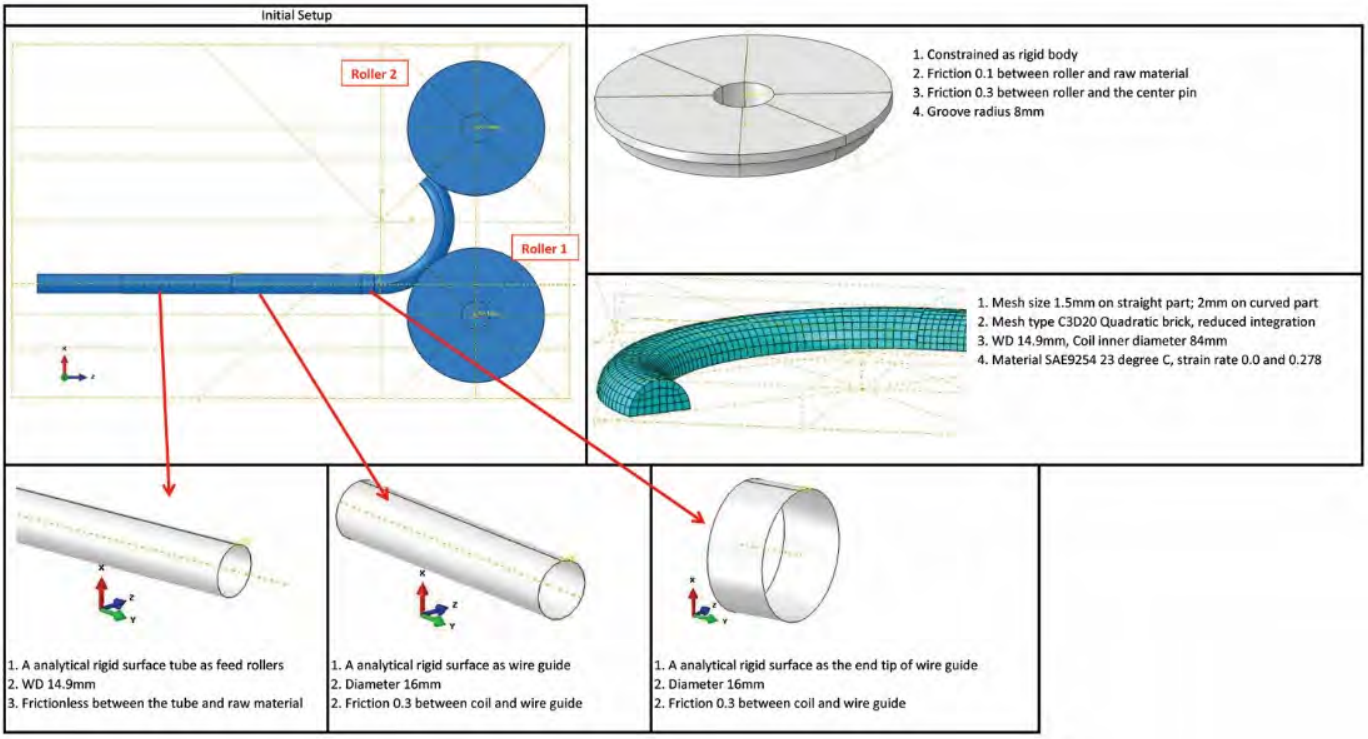


Figure 3. Initial set-up of FEA Model

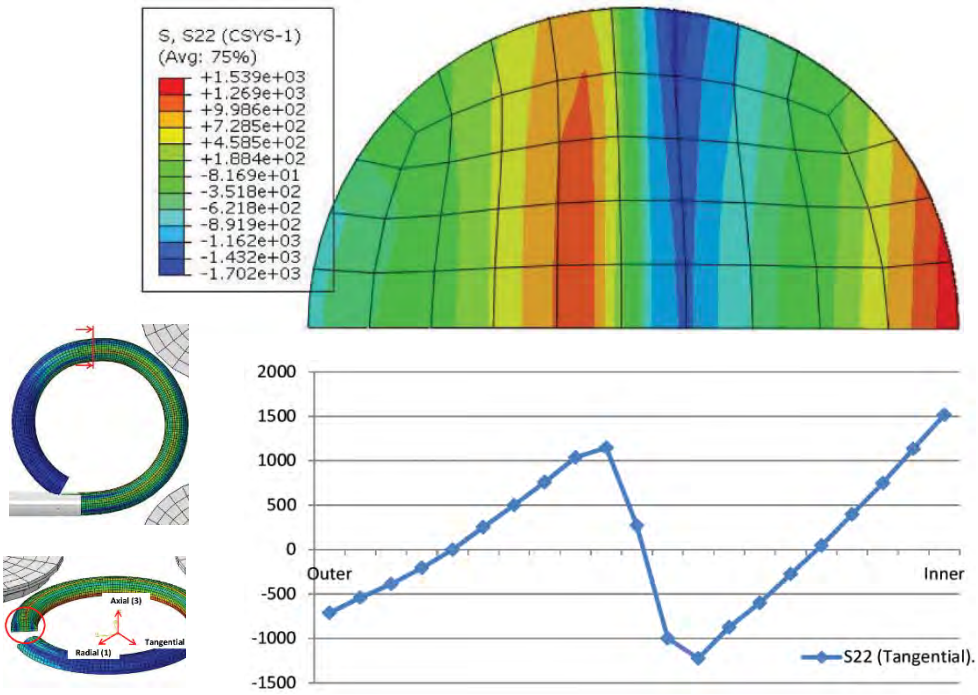


Figure 5. Tangential (wire direction) Residual Stress Distribution.

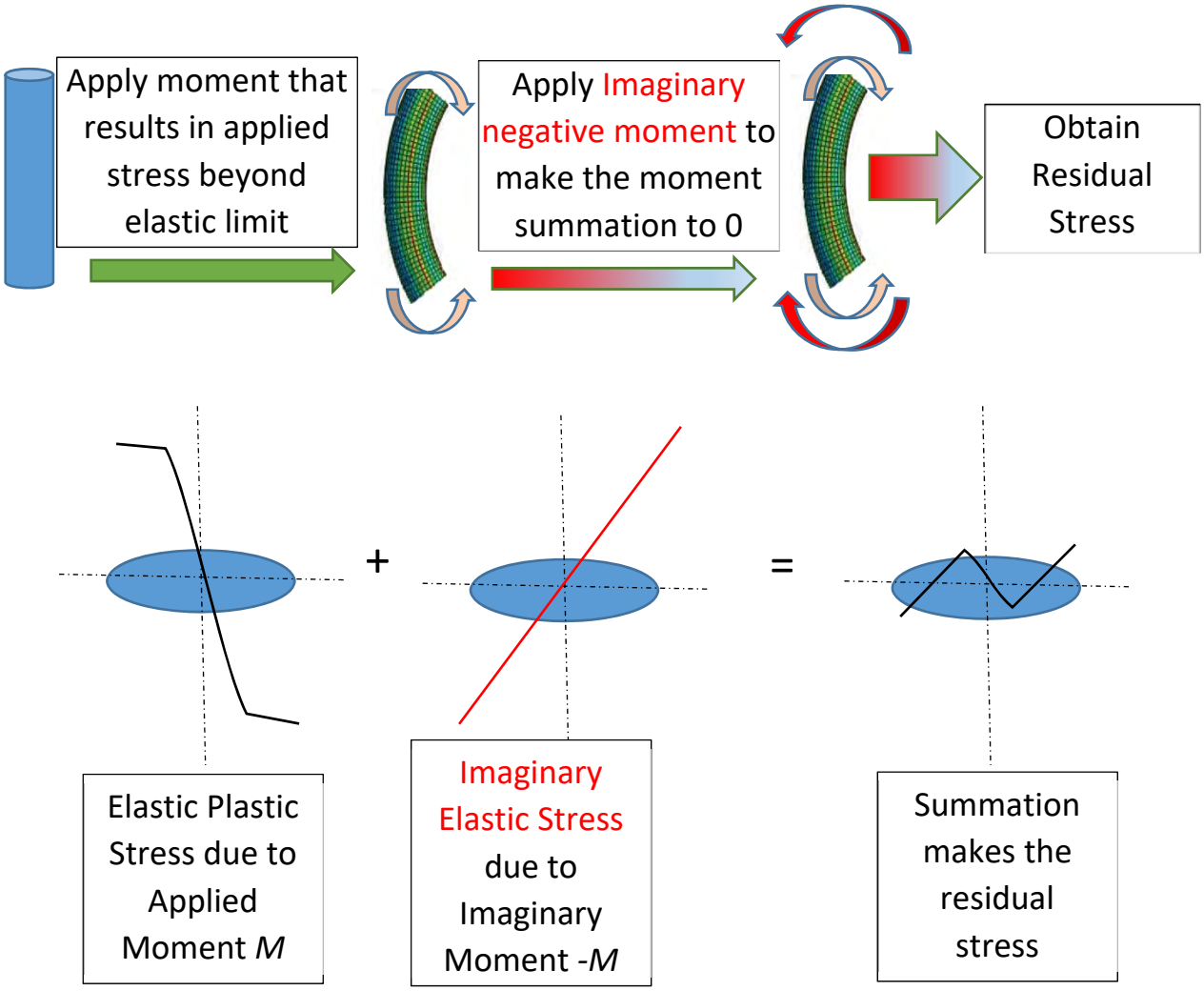


Figure 5. Illustration of tangential stresses at the wire, note that the imaginary moment only creates elastic stress

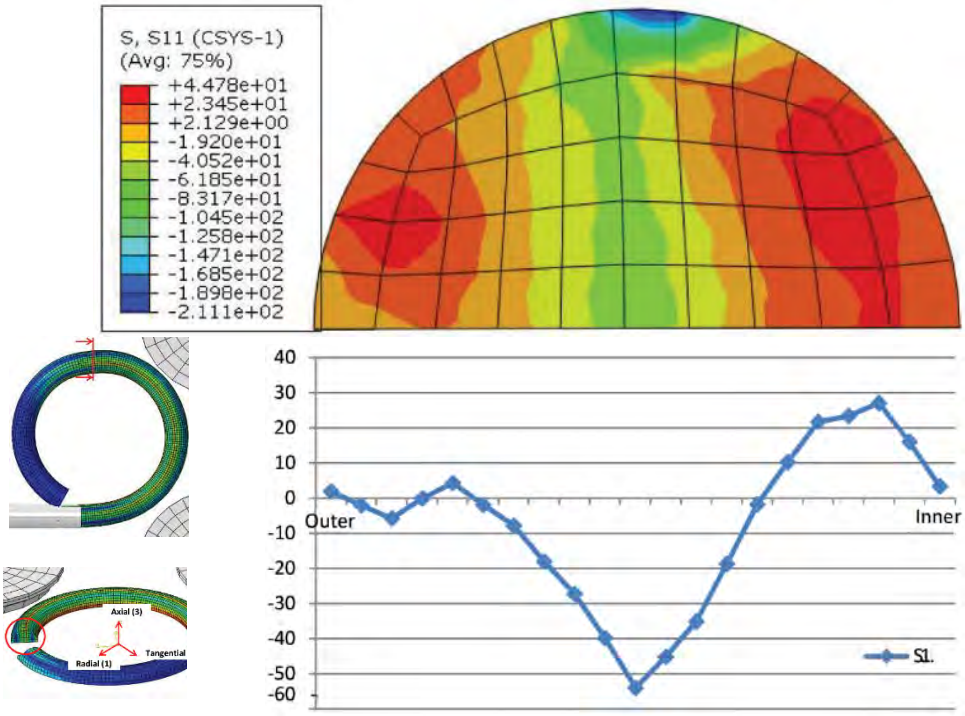


Figure 6. Radial (Coil radius direction) residual stress distribution. In here, this stress is related directly to Mode I of fracture mechanics.

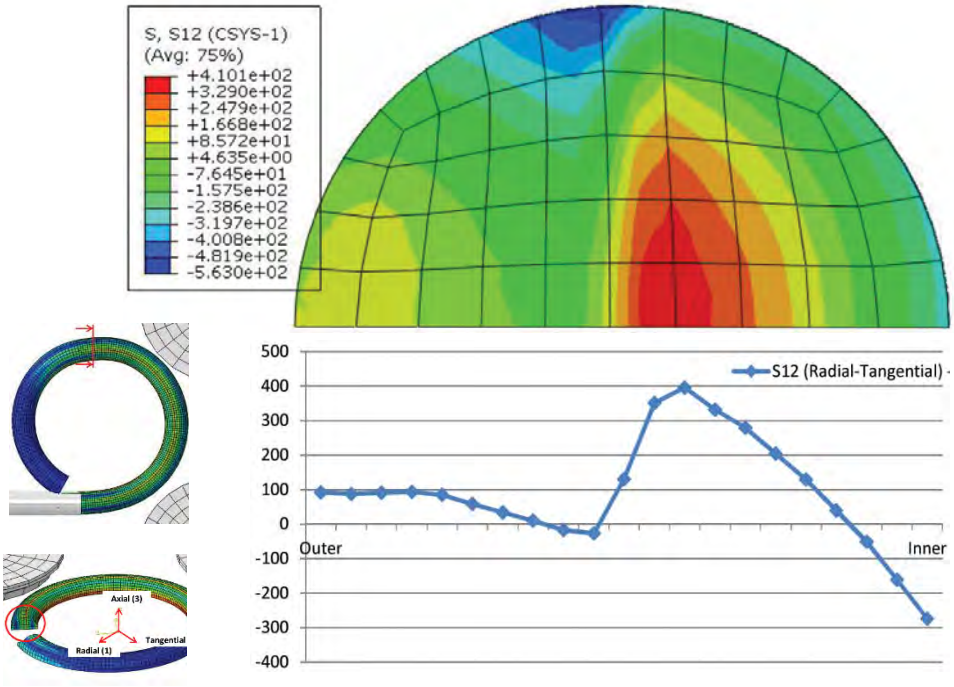


Figure 7. Shear (Radial-Plane;Tangential-direction) residual stress distribution. In here, this stress is related directly to Mode II of fracture mechanics.

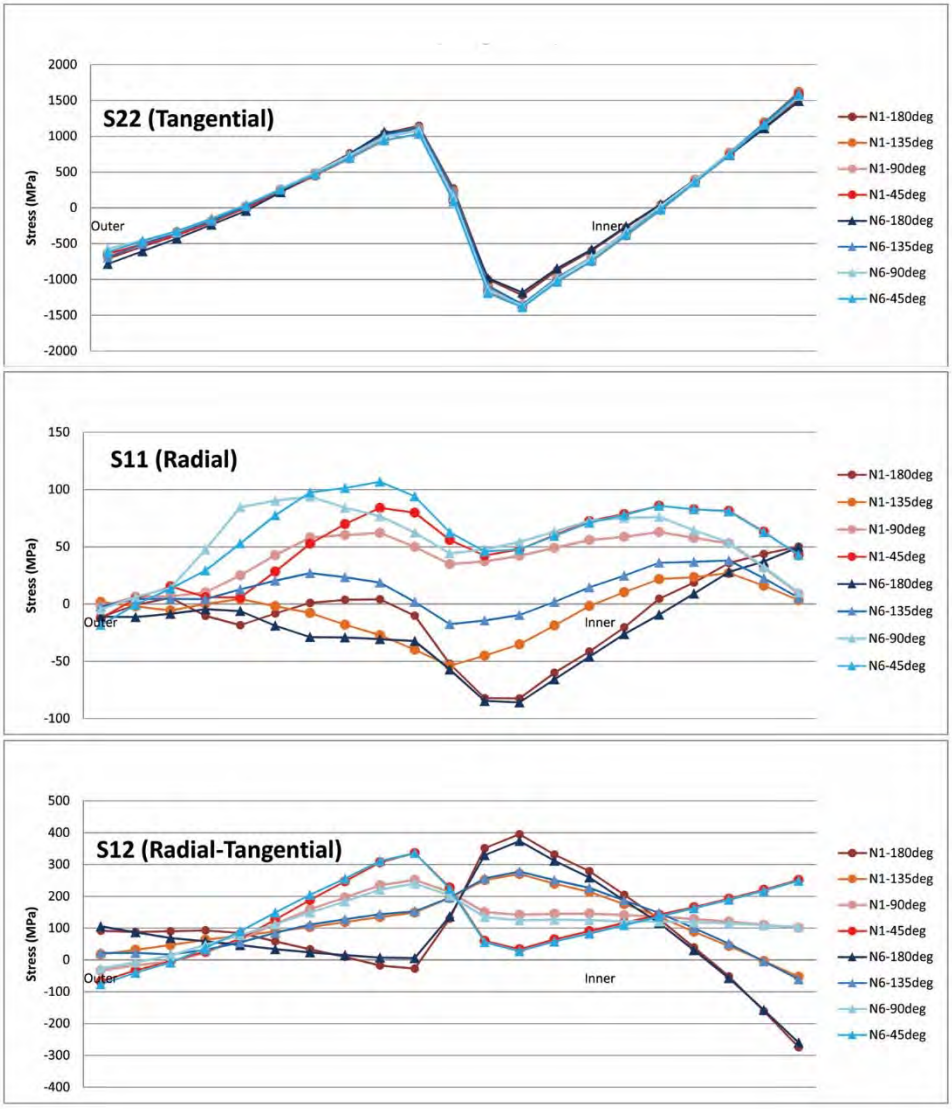


Figure 8. Summary of the analysis results. The comparison here is based on the models constructed to match profiles of N1 and N6 coils.

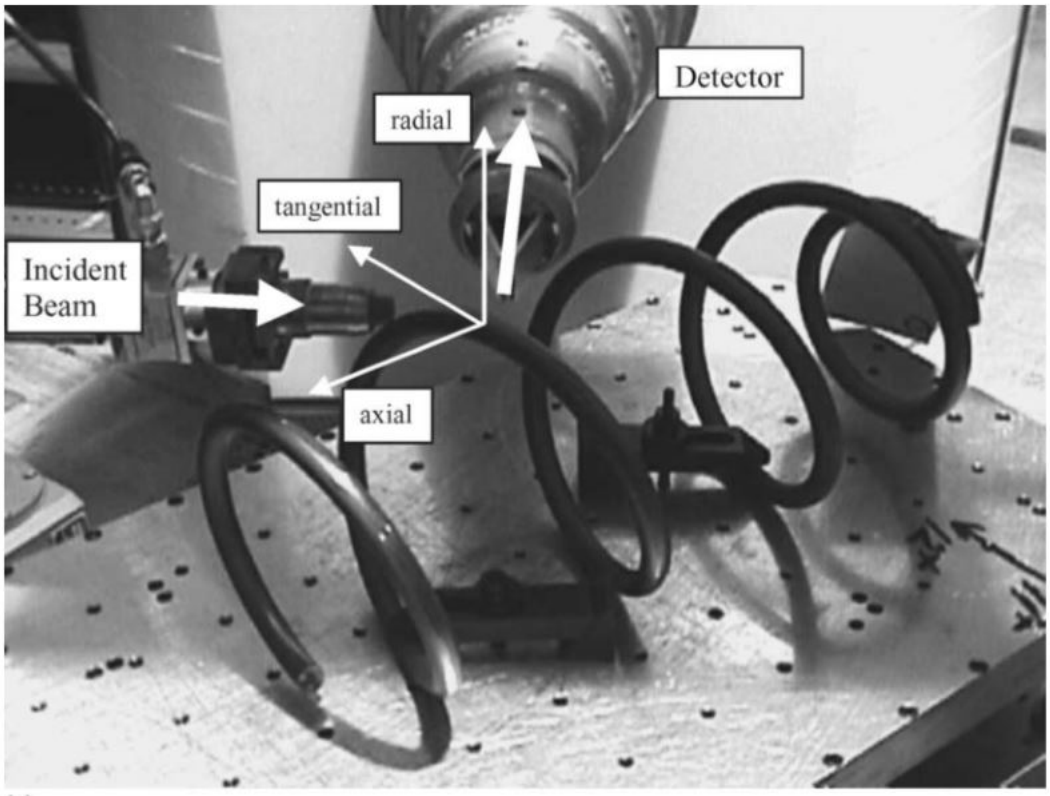


Figure 9. Measurement orientation is to mimic the measurement of Matejicek's[3]. The lower diagram shows the coordinate and points of measurements.

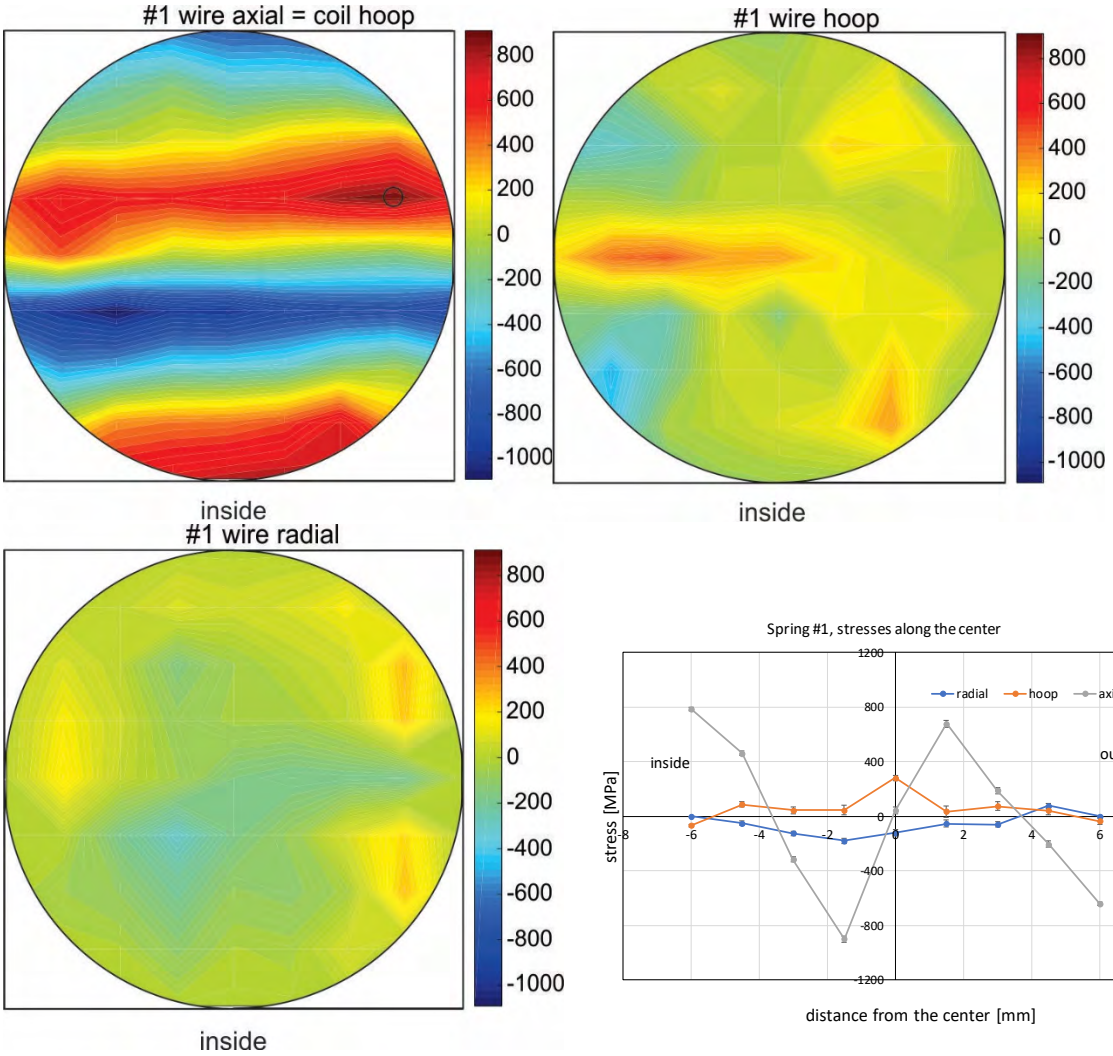


Figure 10a. Neutron diffraction measurement results for spring N1

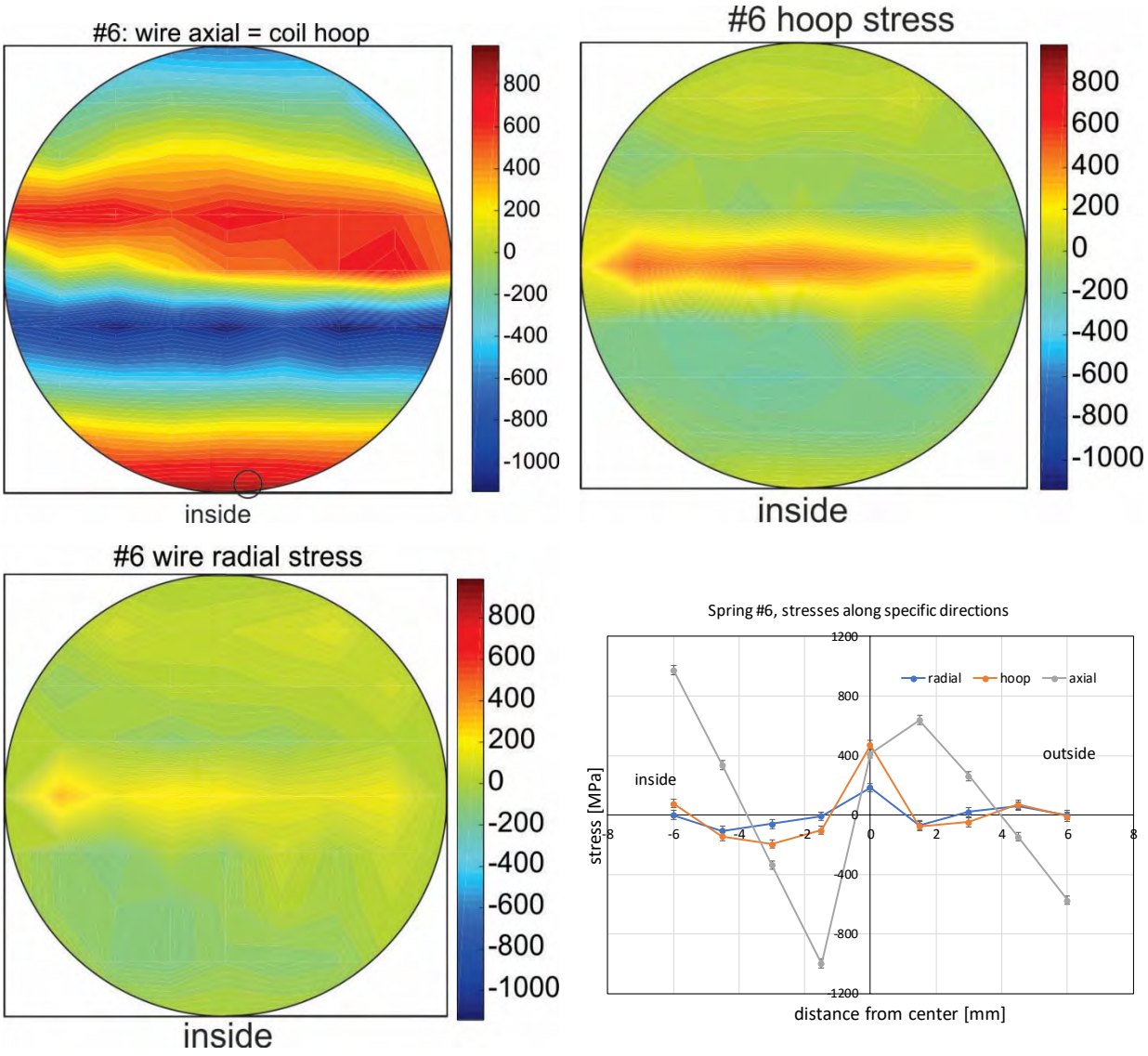


Figure 10b. Neutron diffraction measurement results for spring N6

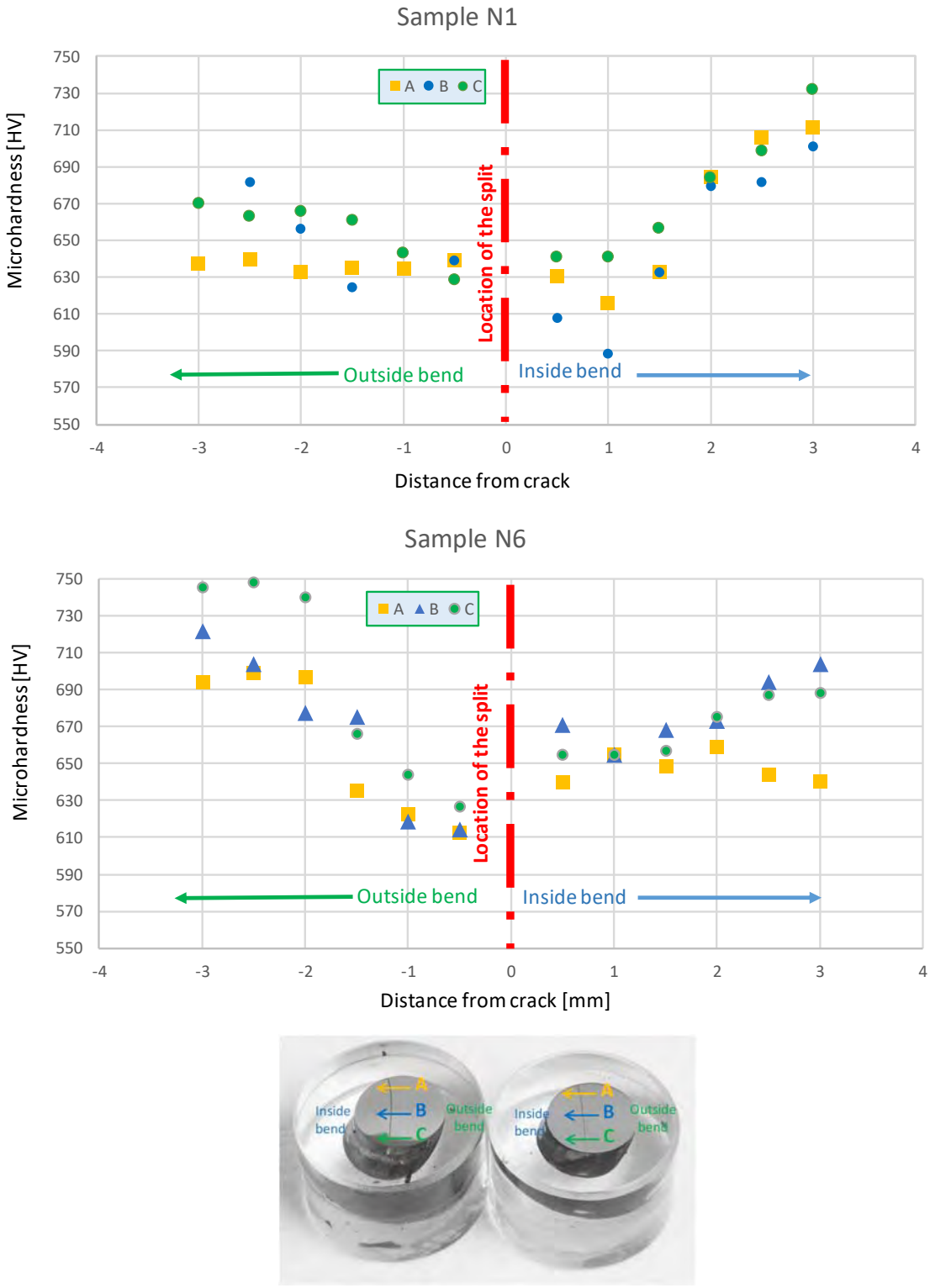


Figure 11. Micro hardness mapping on the samples along three different paths

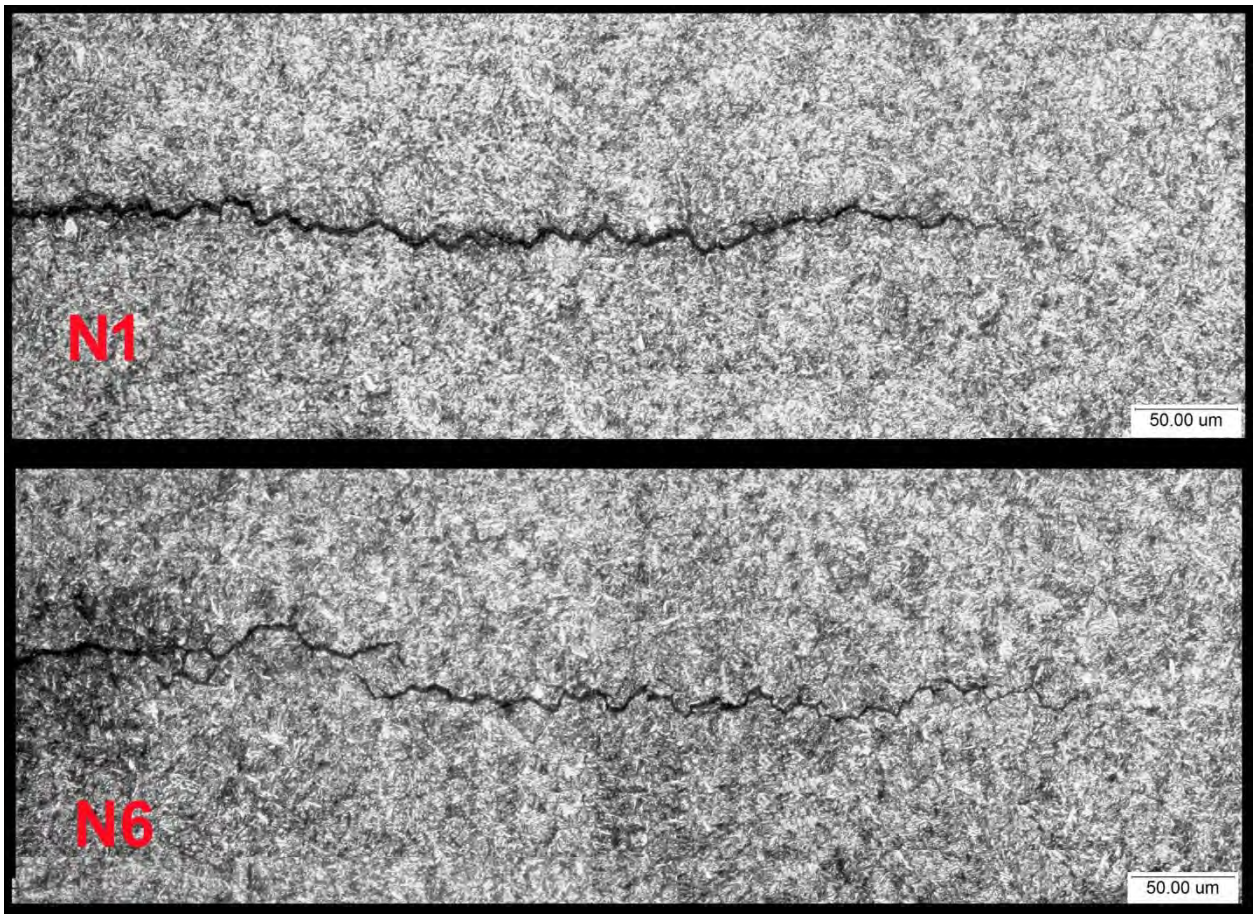




Figure 11. Metallurgical evaluation at the crack tips. N6 sample shows more crack branching, which is an indication of less (applied) stress during the crack formation.

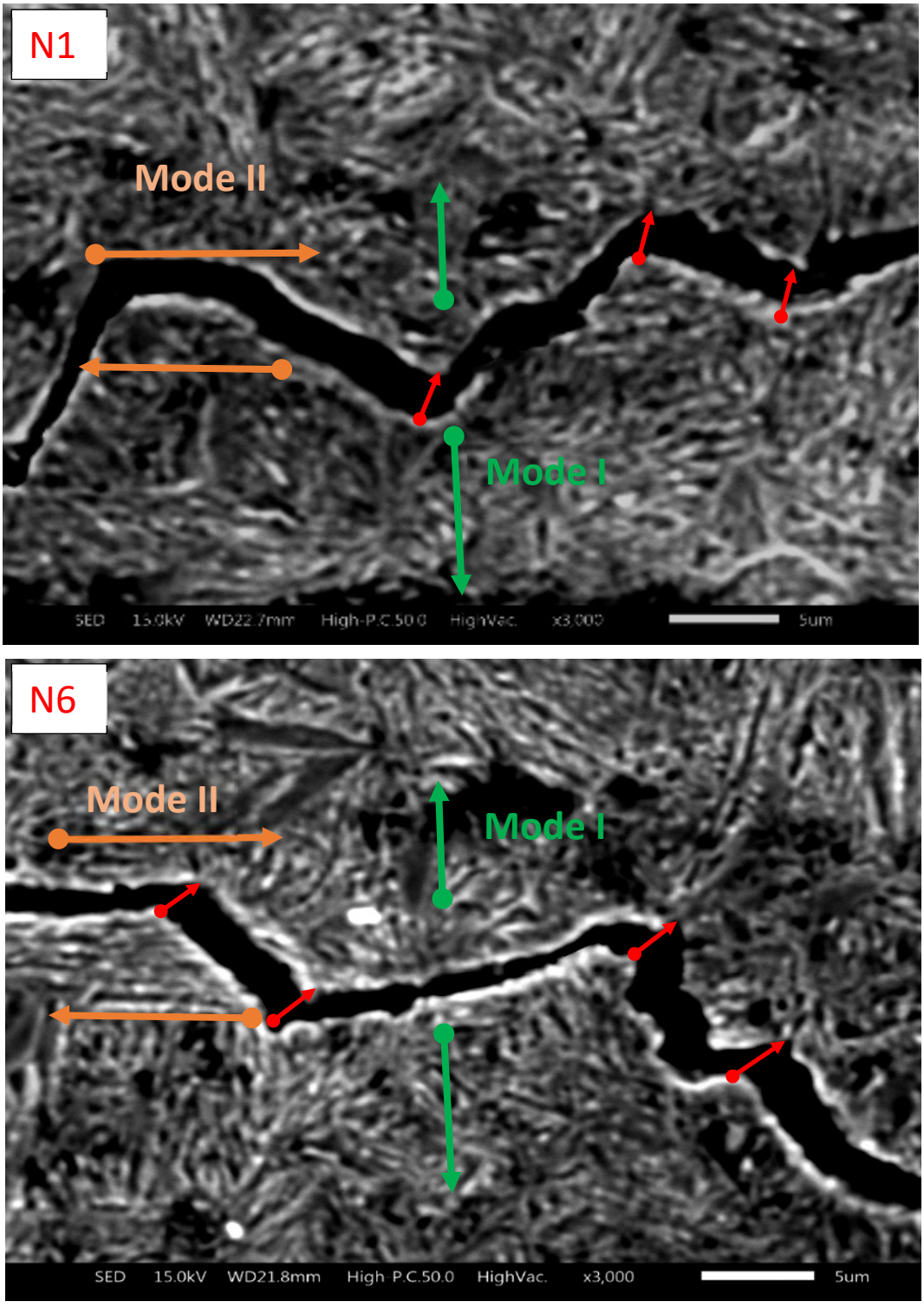


Figure 12. Metallurgical evaluation at selected locations. The appearance here is to confirm that the cracks are indeed influenced by both Mode I (opening) and Mode II (in-plane shear). The red arrows indicate that the translation vector is clearly a combination of Mode I and Mode II.

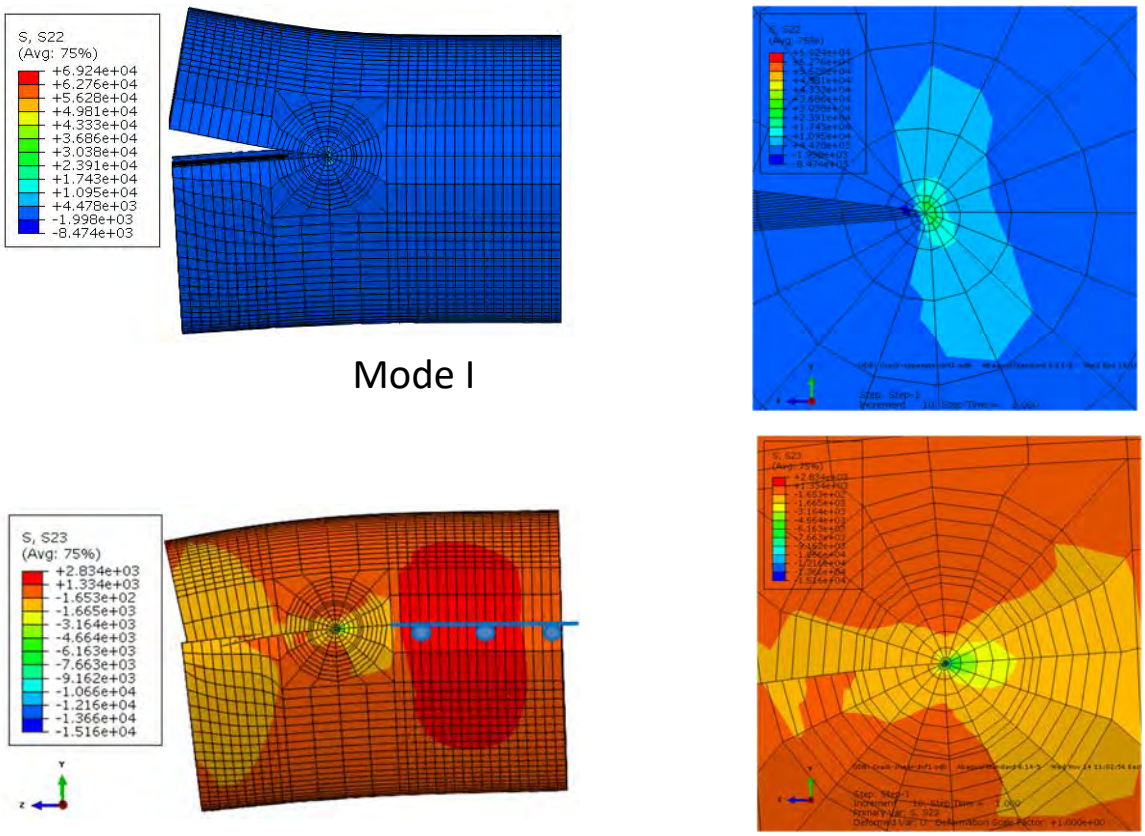


Figure 13. FEA model for the stress intensity calculation. The values of stress intensity factor is taken by the averaging of 5 contours values in front of the crack.

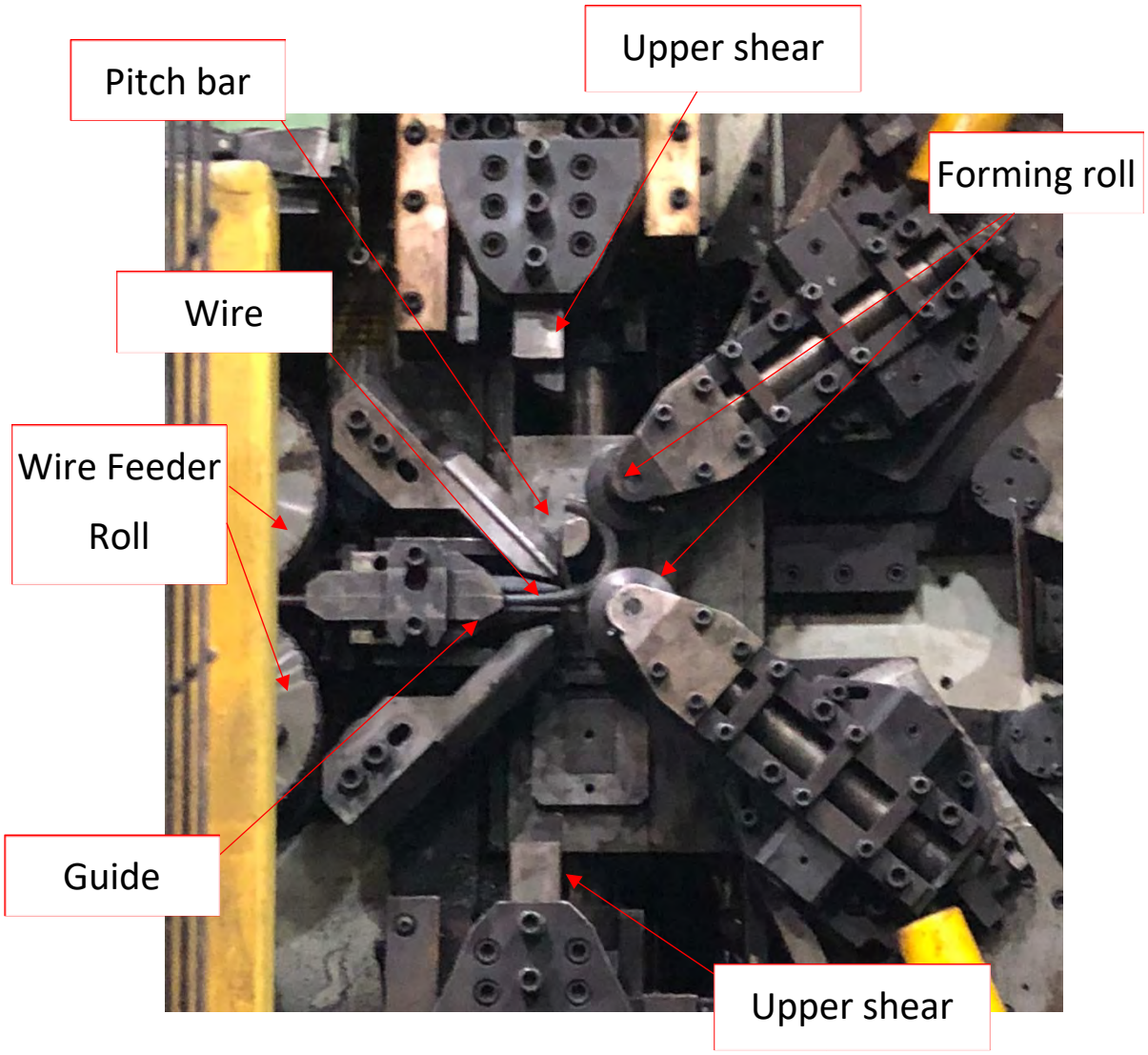


Figure 1. Cold Coiling Machine

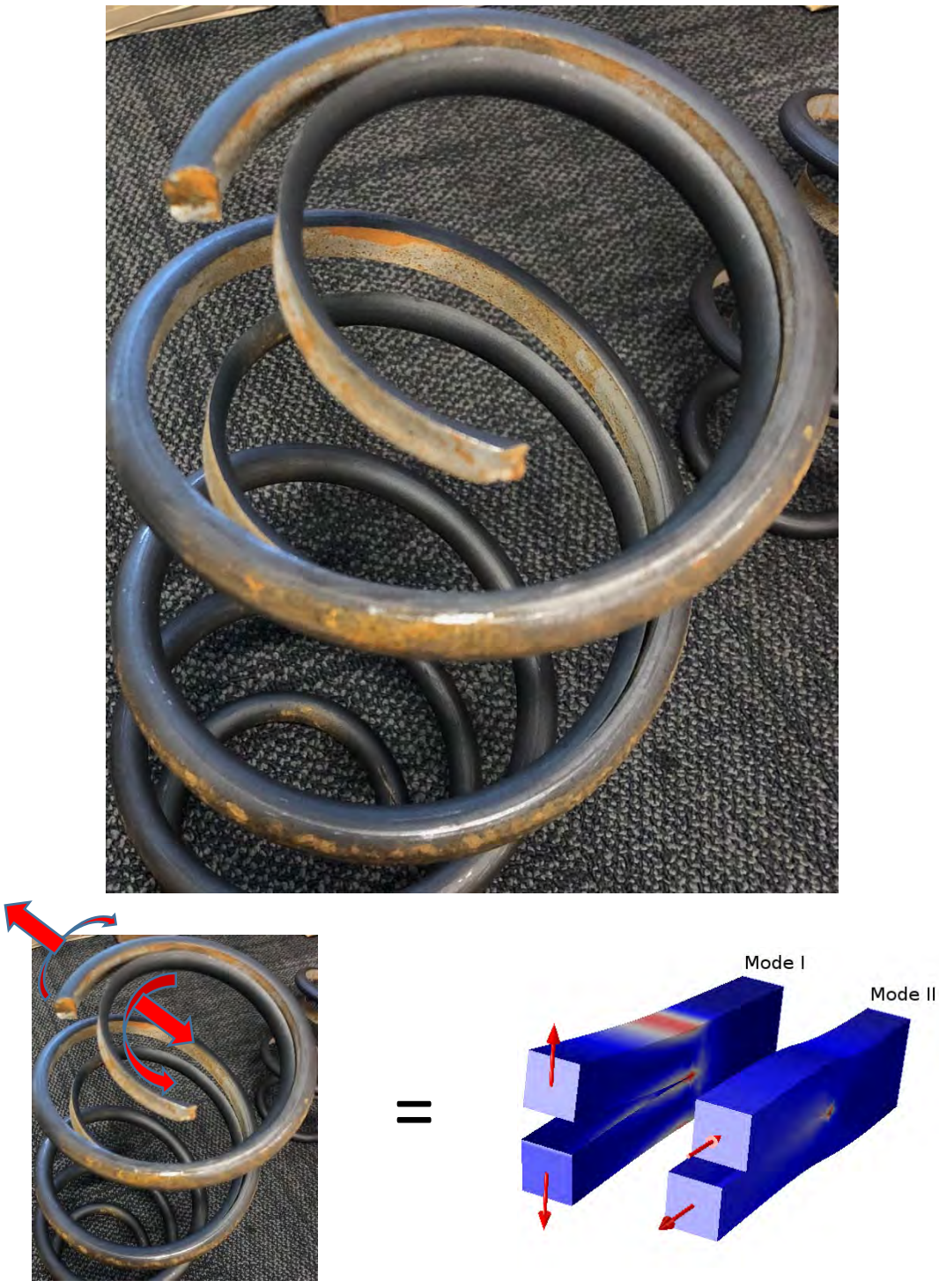


Figure 2. Appearance of the splitting that takes place after coiling before stress relief annealing. The figure also shows the concept for the usage of mixed mode.

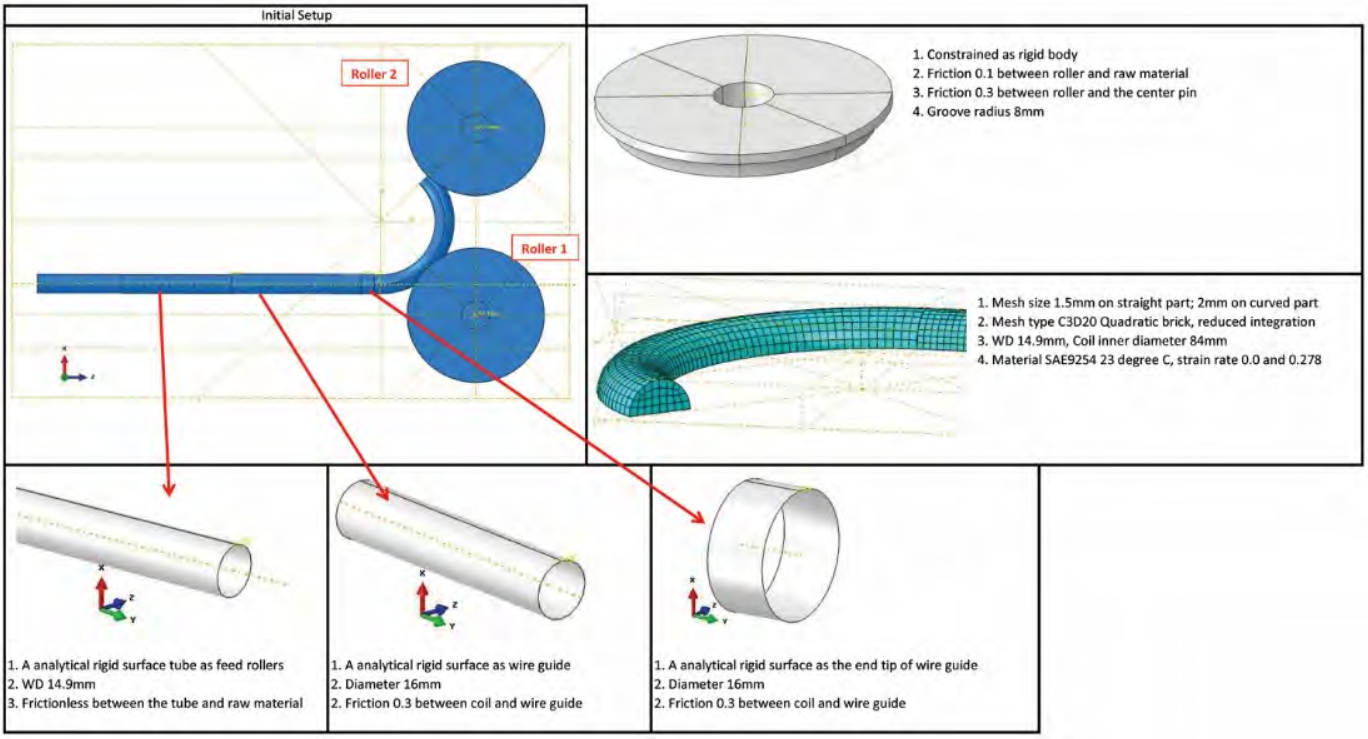


Figure 3. Initial set-up of FEA Model

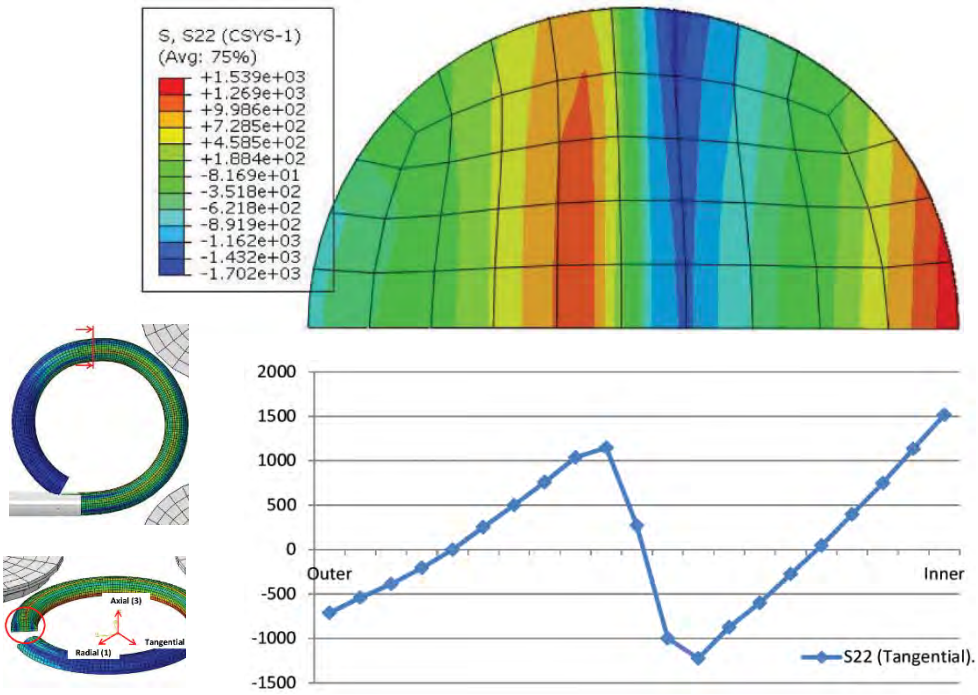


Figure 4. Tangential (wire direction) Residual Stress Distribution.

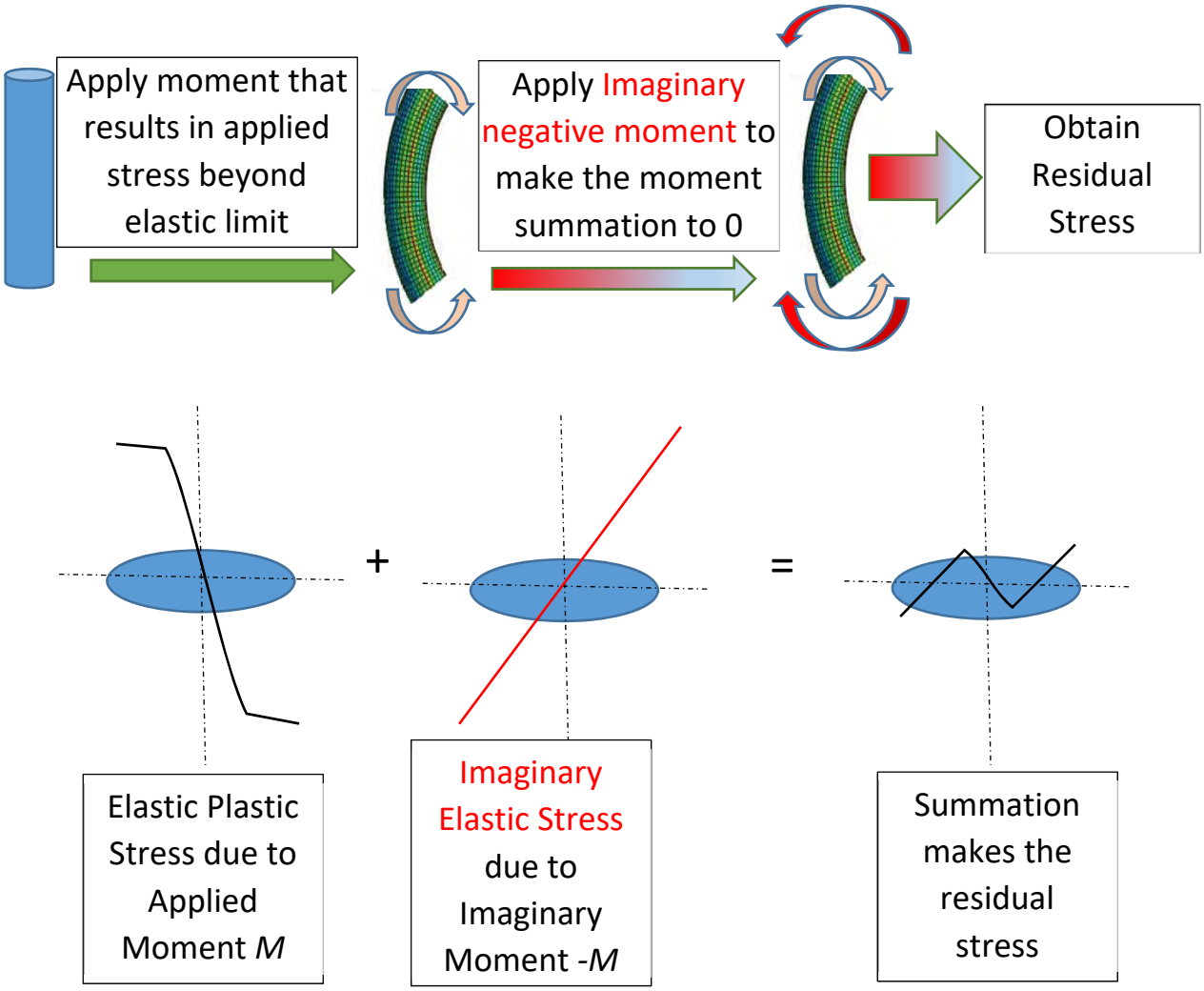


Figure 5. Illustration of tangential stresses at the wire, note that the imaginary moment only creates elastic stress

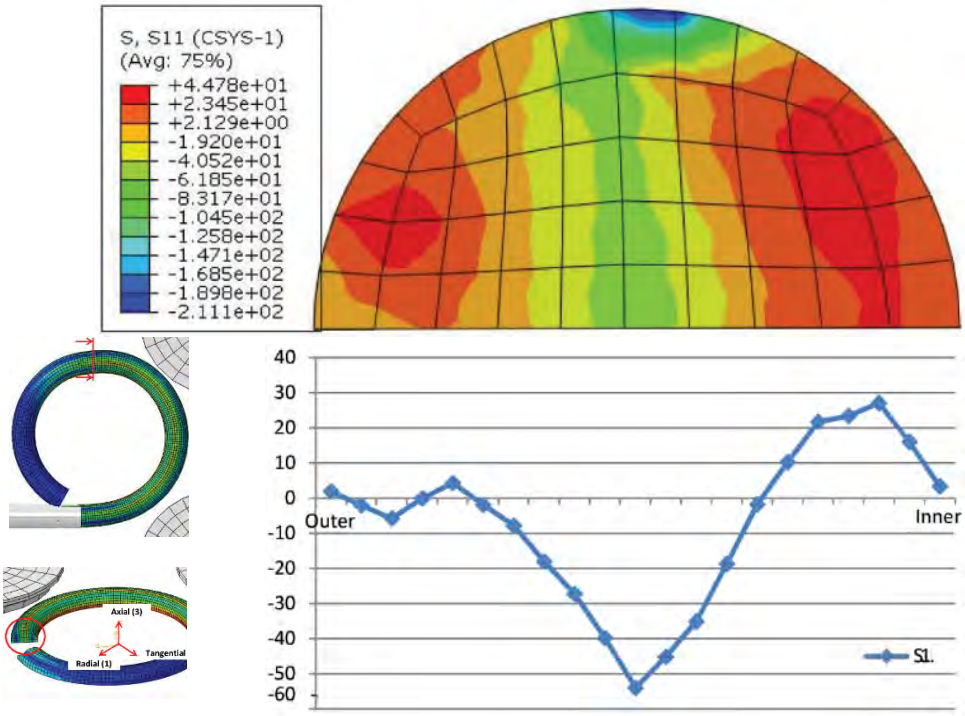


Figure 6. Radial (Coil radius direction) residual stress distribution. In here, this stress is related directly to Mode I of fracture mechanics.

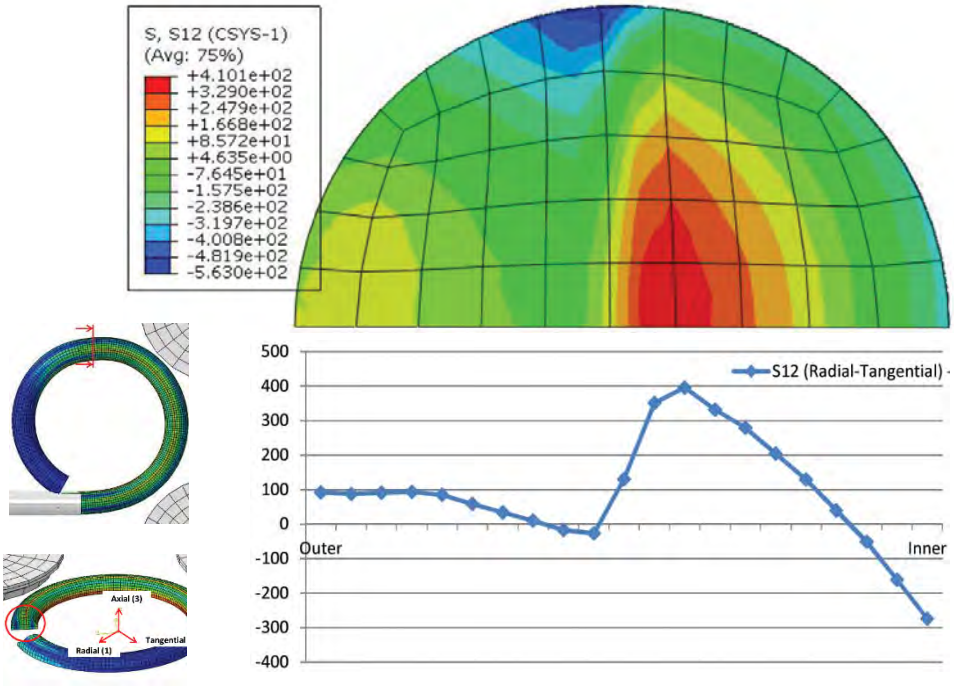


Figure 7. Shear (Radial-Plane;Tangential-direction) residual stress distribution. In here, this stress is related directly to Mode II of fracture mechanics.

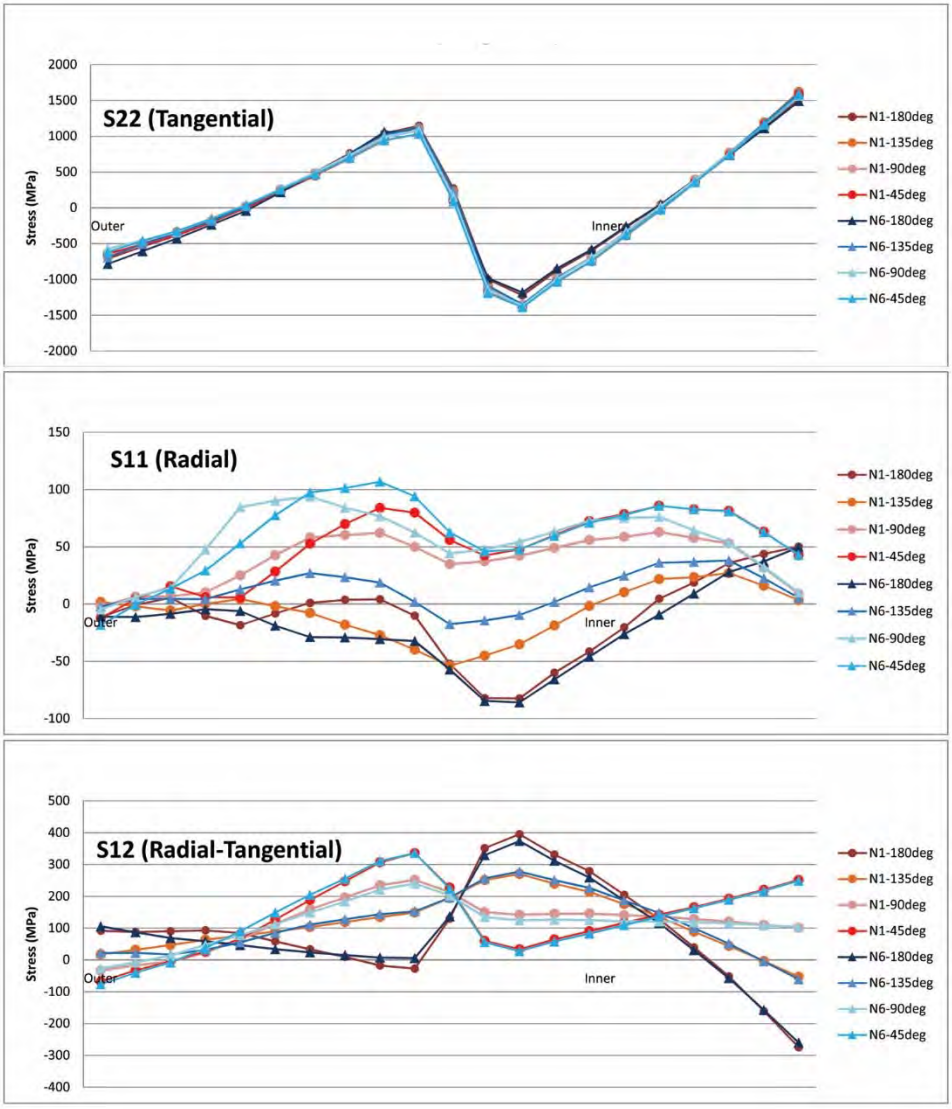


Figure 8. Summary of the analysis results. The comparison here is based on the models constructed to match profiles of N1 and N6 coils.

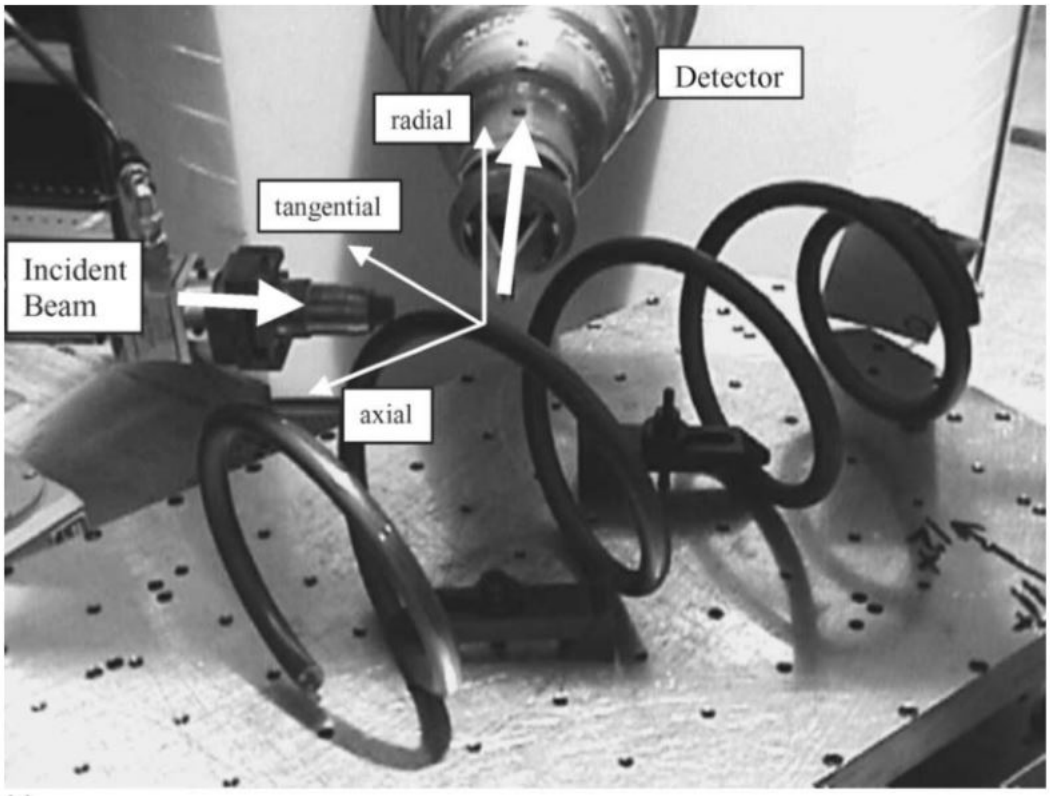


Figure 9. Measurement orientation is to mimic the measurement of Matejicek's[3]. The lower diagram shows the coordinate and points of measurements.

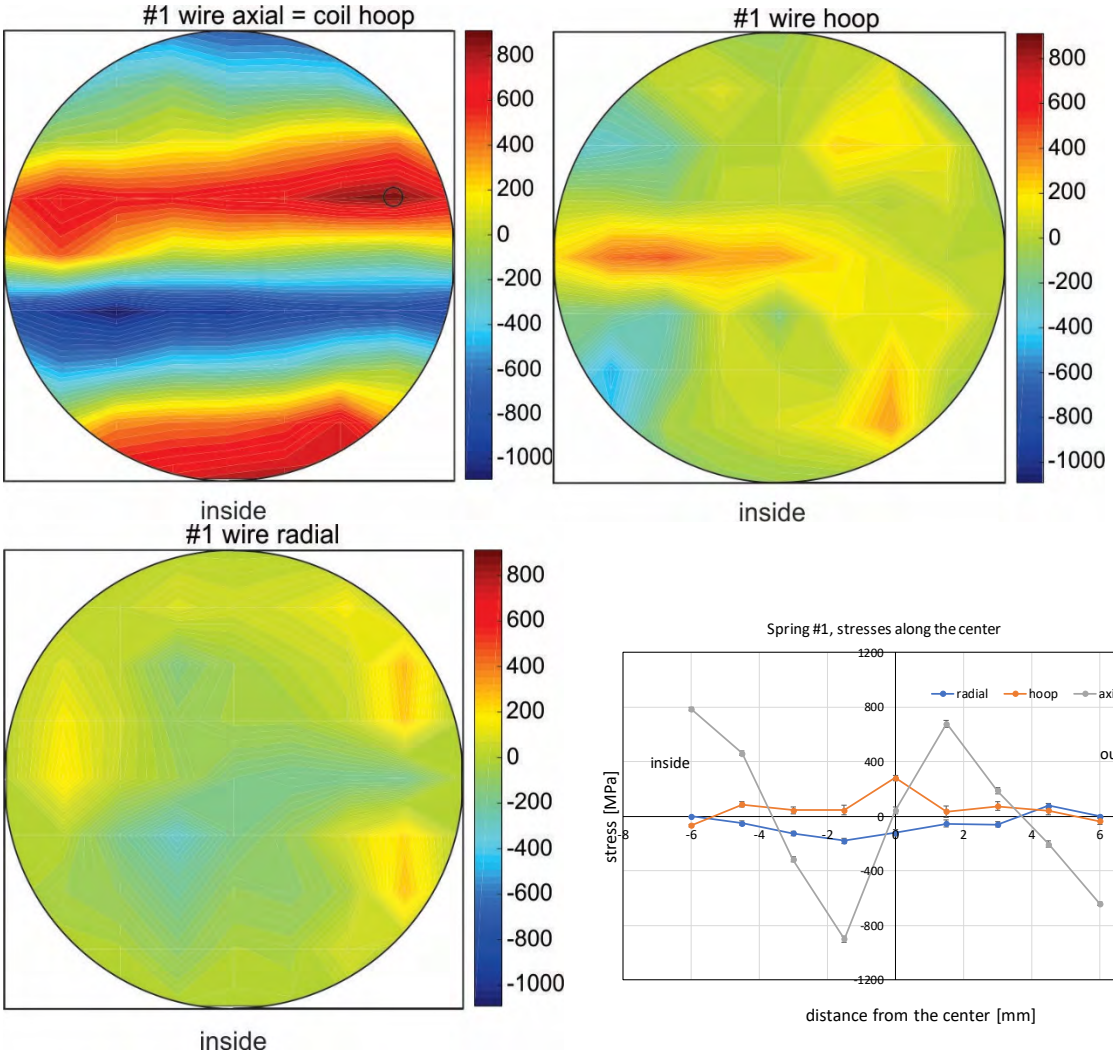


Figure 10a. Neutron diffraction measurement results for spring N1

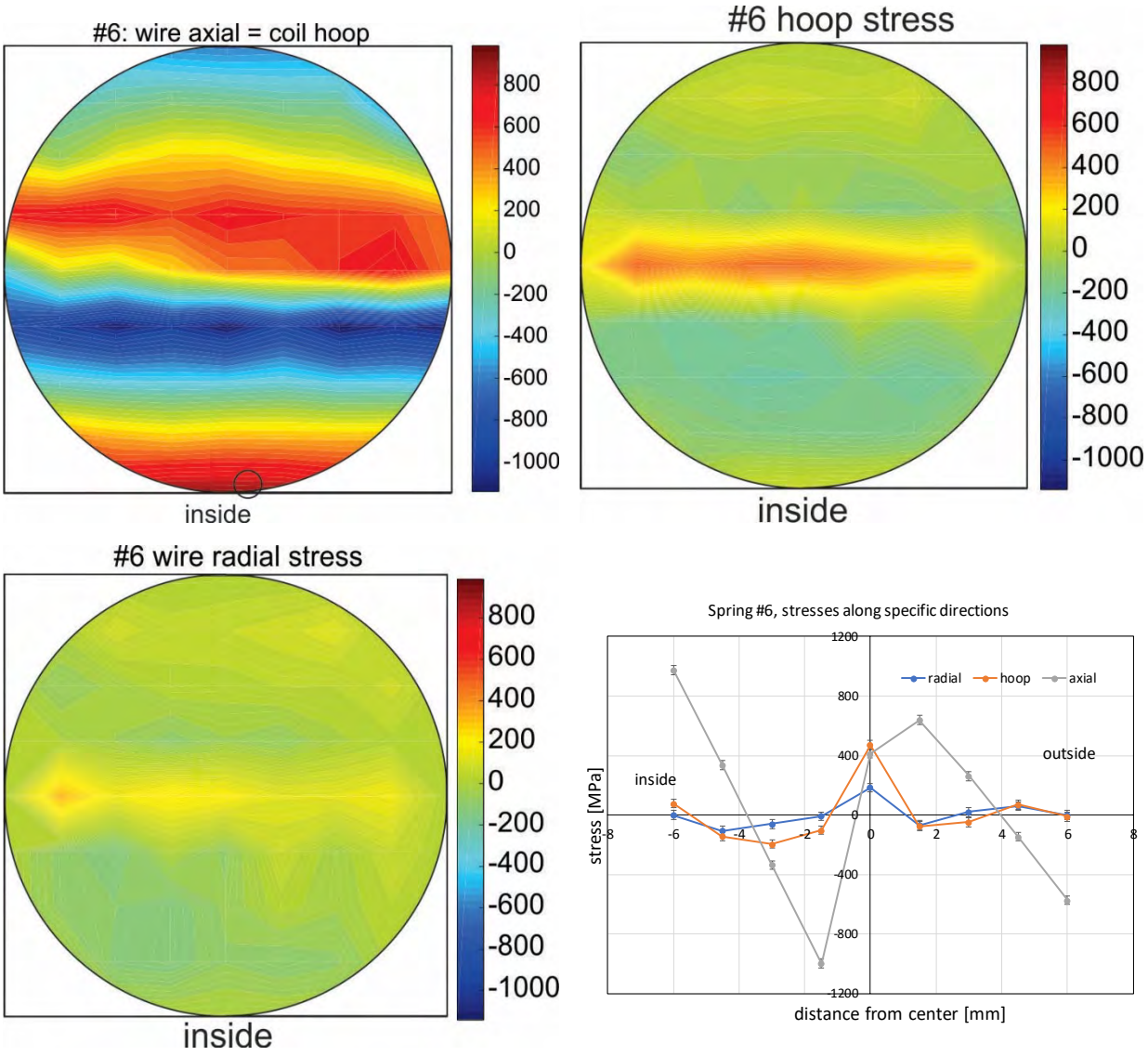


Figure 10b. Neutron diffraction measurement results for spring N6

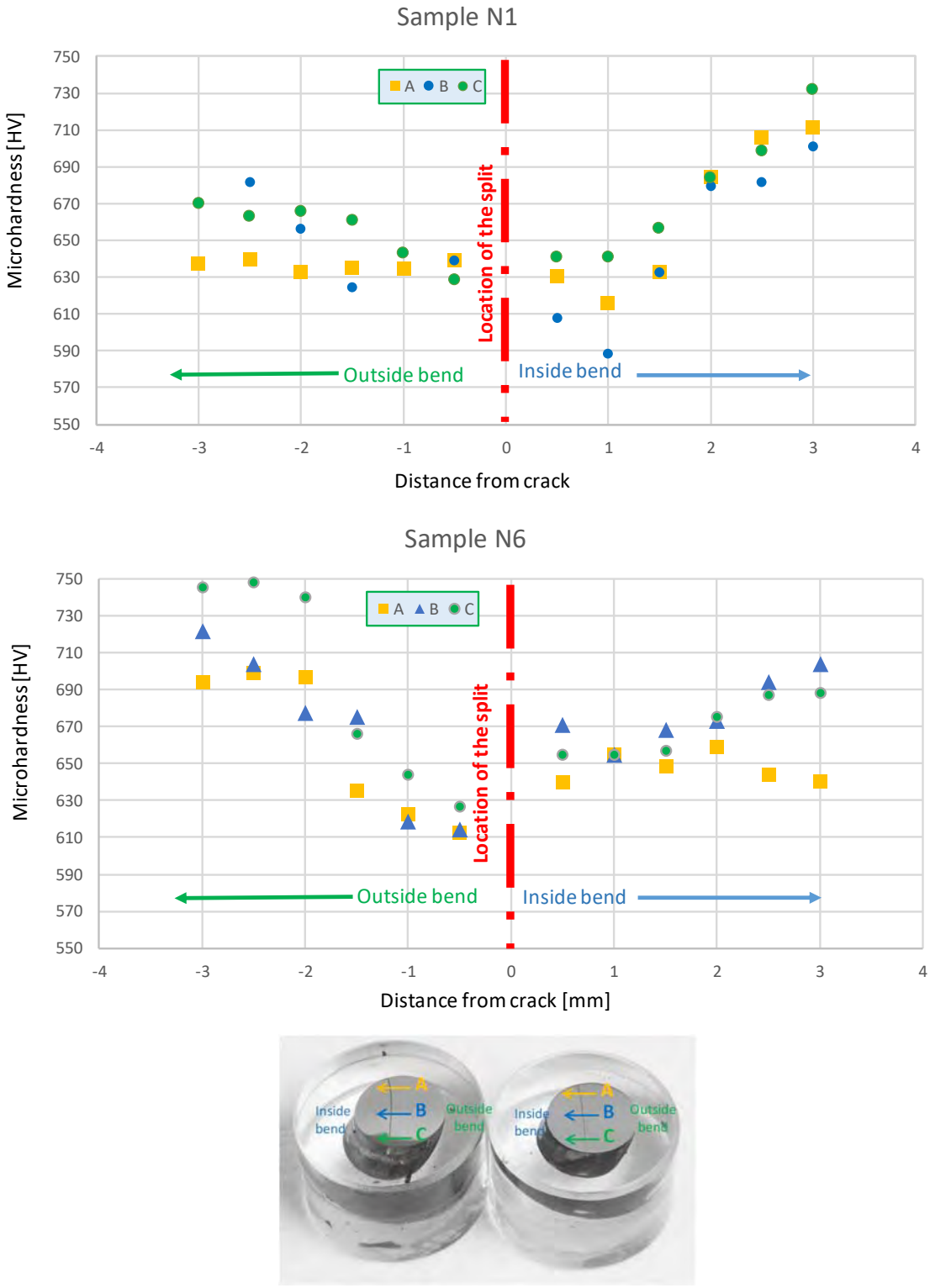


Figure 11. Micro hardness mapping on the samples along three different paths

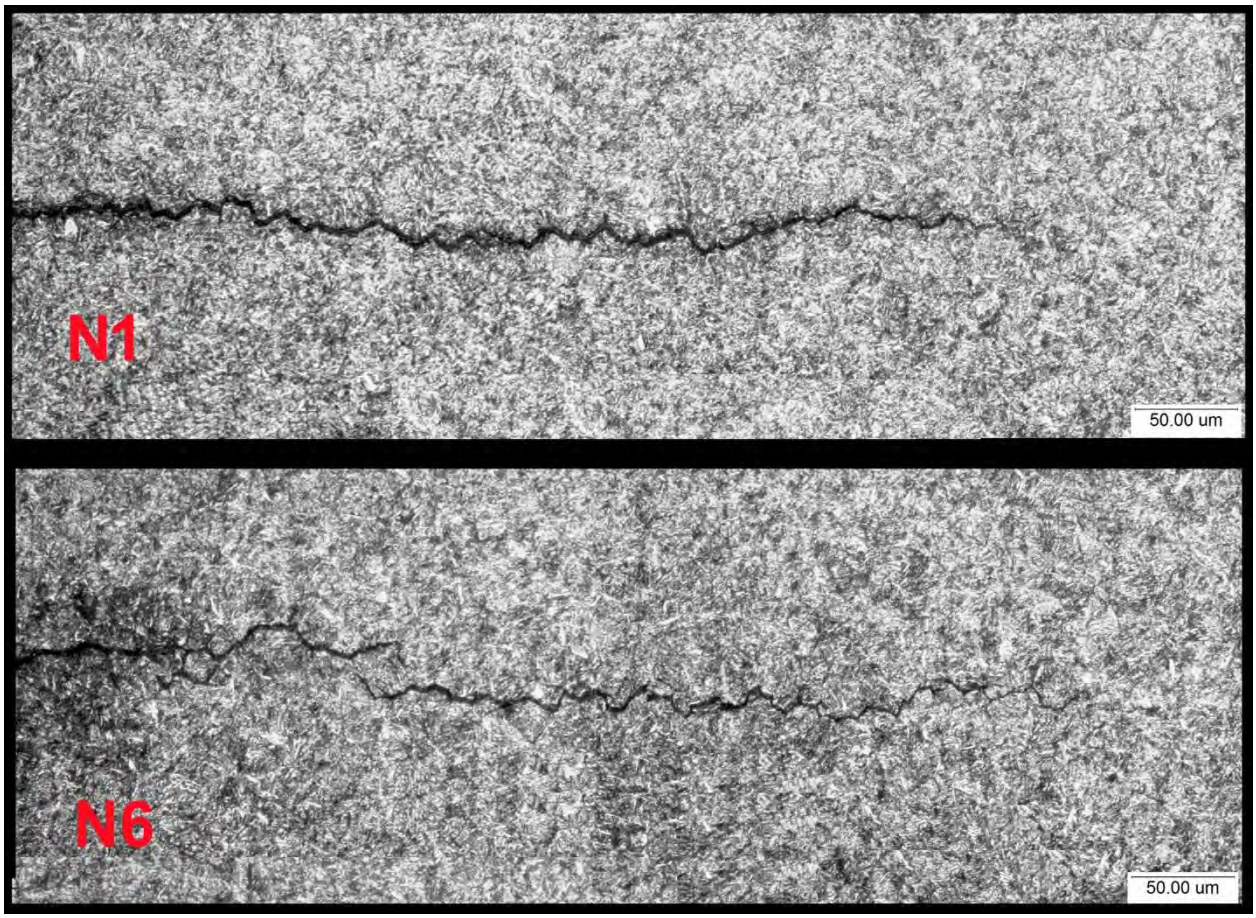




Figure 12. Metallurgical evaluation at the crack tips. N6 sample shows more crack branching, which is an indication of less (applied) stress during the crack formation.

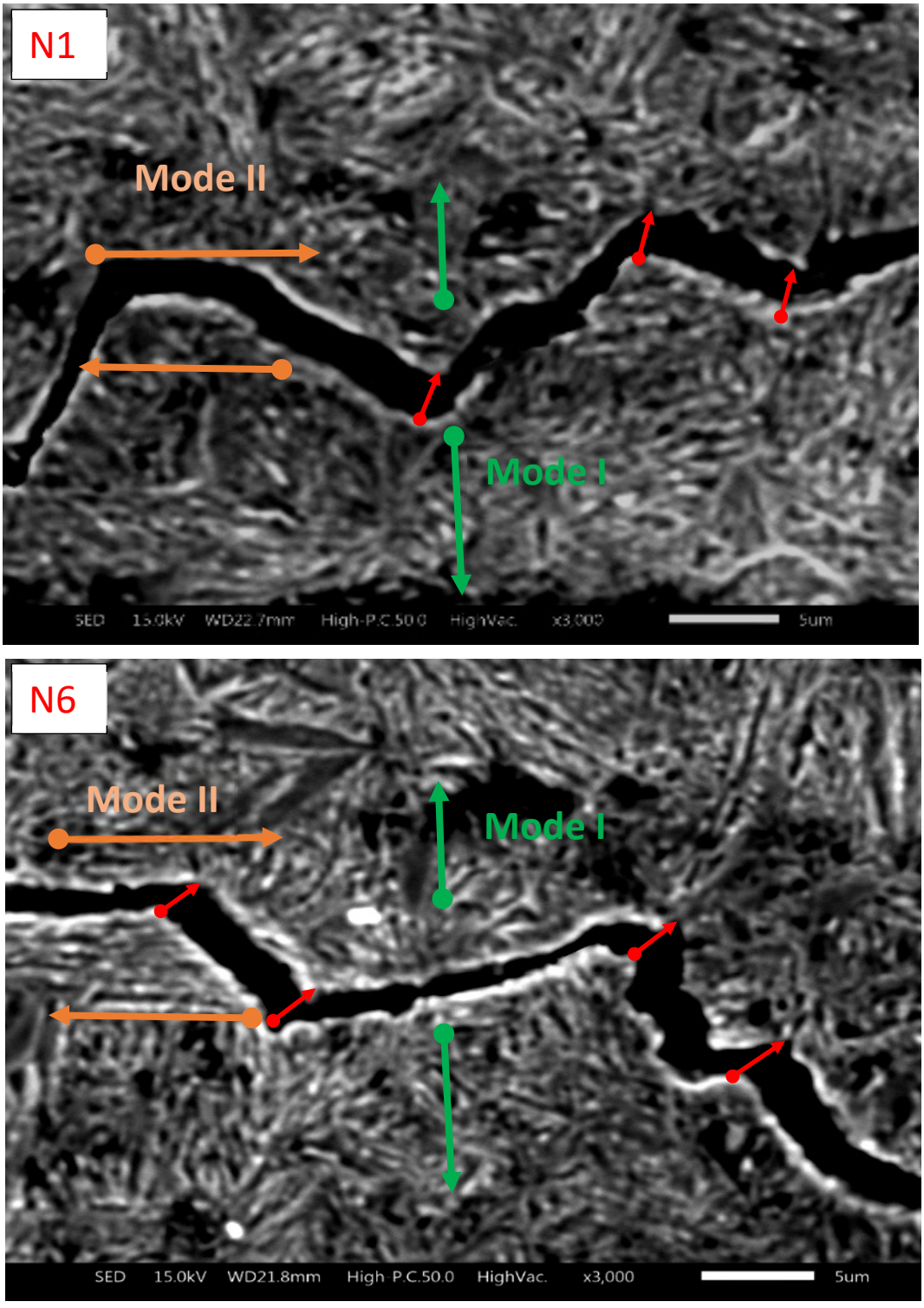


Figure 13. Metallurgical evaluation at selected locations. The appearance here is to confirm that the cracks are indeed influenced by both Mode I (opening) and Mode II (in-plane shear). The red arrows indicate that the translation vector is clearly a combination of Mode I and Mode II.

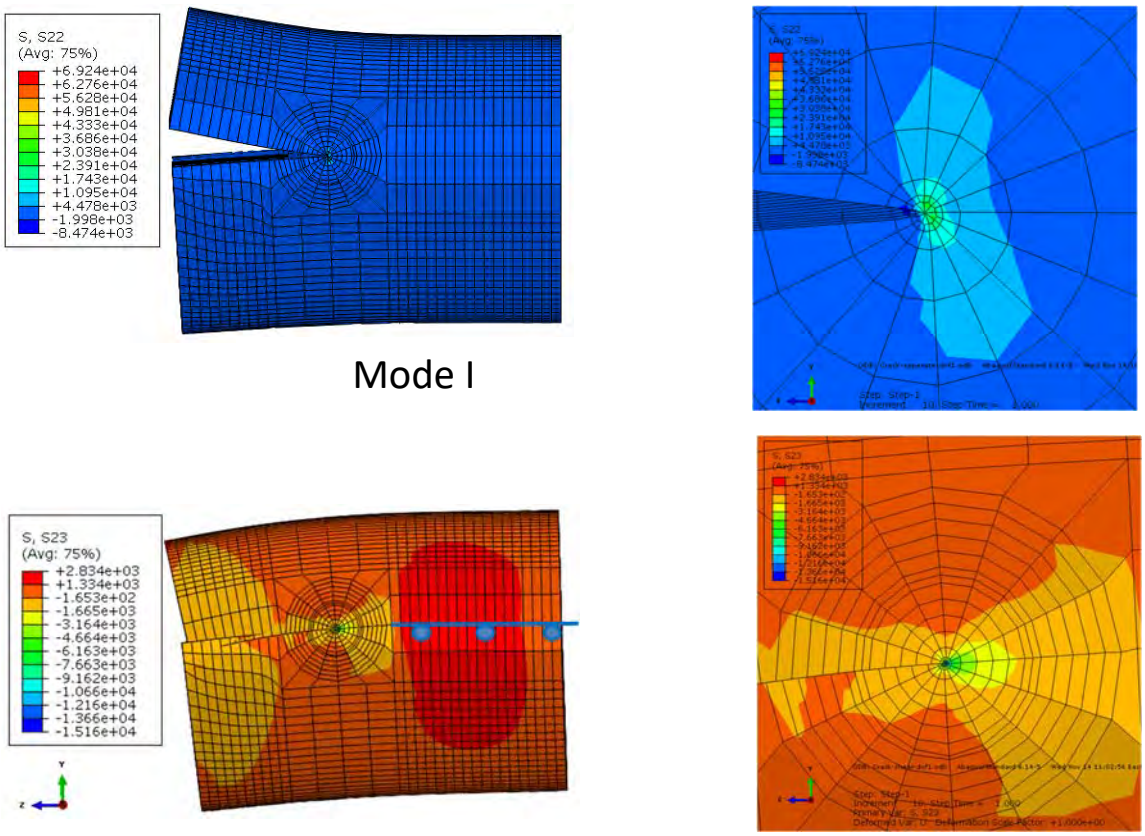


Figure 14. FEA model for the stress intensity calculation. The values of stress intensity factor is taken by the averaging of 5 contours values in front of the crack.